Microglia protect against age-associated brain pathologies

Neuron

Article

Microglia protect against age-associated brain pathologies

Graphical abstract

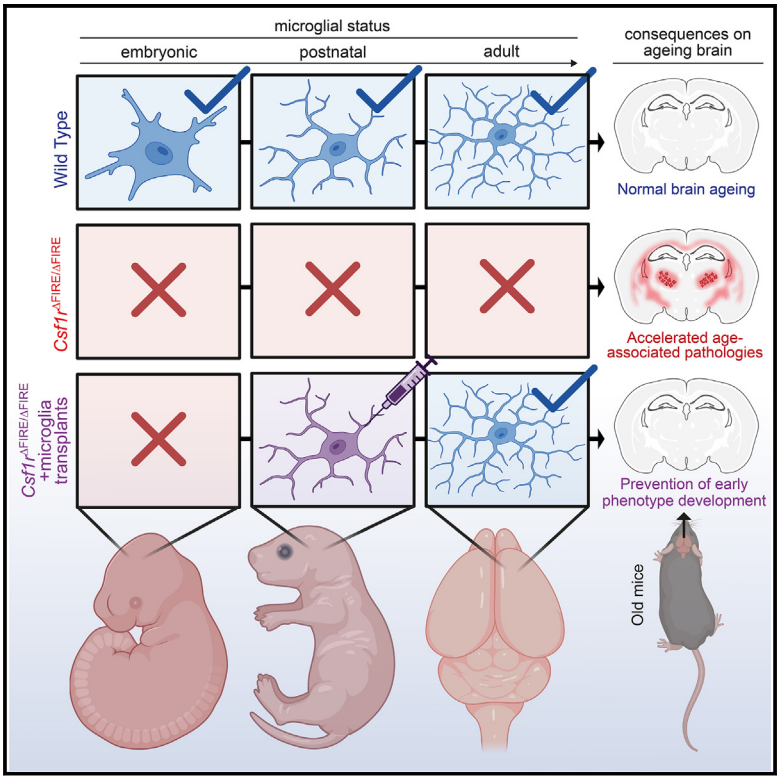

Highlights

- Lack of microglia leads to progressive brain calcifications and macroglial reactivity
- scRNA-seq reveals brain cell profiles across the lifespan in the absence of microglia
- The thalamus is particularly sensitive to the absence of microglia with aging
- Transplanting microglia protects against pathology development

Authors

David A.D. Munro, Nadine Bestard-Cuche, Conor McQuaid, ..., Axel Montagne, Anna Williams, Josef Priller

Correspondence

david.munro@ed.ac.uk (D.A.D.M.), josef.priller@ed.ac.uk (J.P.)

In brief

Microglia are resident immune cells in the brain. Munro et al. explore the consequences of the permanent absence of microglia on the maturation and maintenance of the brain. They show accumulating cellular disruption and damage to the brain as it ages without microglia.

Munro et al., 2024, Neuron *112*, 1–17
August 21, 2024
https://doi.org/10.1016/j.neuron.2024.05.018

CellPress

Neuron

CellPress

Article

Microglia protect against age-associated brain pathologies

David A.D. Munro,[1,2,*] Nadine Bestard-Cuche,[3] Conor McQuaid,[1,2] Audrey Chagnot,[1,2] Sepideh Kiani Shabestari,[4,5] Jean Paul Chadarevian,[4,5,6] Upasana Maheshwari,[7] Stefan Szymkowiak,[1,8] Kim Morris,[1] Mehreen Mohammad,[1] Andrea Corsinotti,[3] Barry Bradford,[9] Neil Mabbott,[9] Ross J. Lennen,[10] Maurits A. Jansen,[10,11] Clare Pridans,[12] Barry W. McColl,[1,8] Annika Keller,[7,13] Mathew Blurton-Jones,[4,5,6] Axel Montagne,[1,2] Anna Williams,[1,3] and Josef Priller[1,2,14,15,16,*]

[1]UK Dementia Research Institute at the University of Edinburgh, Edinburgh Medical School, Chancellor's Building, Edinburgh EH16 4SB, UK
[2]Centre for Clinical Brain Sciences, University of Edinburgh, Chancellor's Building, 49 Little France Crescent, Edinburgh EH16 4SB, UK
[3]Institute for Regeneration and Repair, University of Edinburgh, Edinburgh EH16 4UU, UK
[4]Department of Neurobiology & Behavior, University of California, Irvine, Irvine, CA 92697, USA
[5]Sue and Bill Gross Stem Cell Research Center, University of California, Irvine, Irvine, CA 92697, USA
[6]Institute for Memory Impairments and Neurological Disorders, University of California, Irvine, Irvine, CA 92697, USA
[7]Department of Neurosurgery, Clinical Neuroscience Center, University Hospital Zurich, University of Zurich, Zurich, Switzerland
[8]Centre for Discovery Brain Sciences, University of Edinburgh, Hugh Robson Building, George Square, Edinburgh EH8 9XD, UK
[9]The Roslin Institute and R(D)SVS, University of Edinburgh, Easter Bush Campus, Midlothian, UK
[10]Centre for Cardiovascular Science, University of Edinburgh, Queen's Medical Research Institute, Edinburgh EH16 4TJ, UK
[11]Department of Radiology and Medical Imaging, University of Virginia, Charlottesville, VA, USA
[12]Centre for Inflammation Research, Institute for Regeneration and Repair, University of Edinburgh, Edinburgh, UK
[13]Neuroscience Center Zurich, University of Zurich and ETH Zurich, Zurich, Switzerland
[14]Department of Psychiatry and Psychotherapy, School of Medicine and Health, Klinikum rechts der Isar, Technical University Munich, and German Center for Mental Health (DZPG), 81675 Munich, Germany
[15]Neuropsychiatry and Laboratory of Molecular Psychiatry, Charité – Universitätsmedizin Berlin and DZNE, 10117 Berlin, Germany
[16]Lead contact
*Correspondence: david.munro@ed.ac.uk (D.A.D.M.), josef.priller@ed.ac.uk (J.P.)
https://doi.org/10.1016/j.neuron.2024.05.018

SUMMARY

Microglia are brain-resident macrophages that contribute to central nervous system (CNS) development, maturation, and preservation. Here, we examine the consequences of permanent microglial deficiencies on brain aging using the *Csf1r*$^{\Delta FIRE/\Delta FIRE}$ mouse model. In juvenile *Csf1r*$^{\Delta FIRE/\Delta FIRE}$ mice, we show that microglia are dispensable for the transcriptomic maturation of other brain cell types. By contrast, with advancing age, pathologies accumulate in *Csf1r*$^{\Delta FIRE/\Delta FIRE}$ brains, macroglia become increasingly dysregulated, and white matter integrity declines, mimicking many pathological features of human CSF1R-related leukoencephalopathy. The thalamus is particularly vulnerable to neuropathological changes in the absence of microglia, with atrophy, neuron loss, vascular alterations, macroglial dysregulation, and severe tissue calcification. We show that populating *Csf1r*$^{\Delta FIRE/\Delta FIRE}$ brains with wild-type microglia protects against many of these pathological changes. Together with the accompanying study by Chadarevian and colleagues[1], our results indicate that the lifelong absence of microglia results in an age-related neurodegenerative condition that can be counteracted via transplantation of healthy microglia.

INTRODUCTION

Microglia, the resident macrophages of the brain parenchyma, carry out diverse roles within the embryonic and adult central nervous system (CNS).[2] Their specialized signatures emerge progressively during development and are thought to be promoted and maintained in adulthood through the effects of other brain cells.[3–5] Reciprocally, microglia may promote the maturation and maintenance of other brain cells, such as macroglia and neuronal cells,[6–9] but this is incompletely understood.

To understand the role of microglia on the maturation and maintenance of brain cells, we investigated brain aging in a microglia-deficient mouse model. Colony stimulating factor 1 receptor (CSF1R) is essential for microglial survival, and its expression is controlled by the *fms*-intronic regulatory enhancer (FIRE), a highly conserved super-enhancer within intron 2 of the gene.[10,11] Mice generated to lack the FIRE element (*Csf1r*$^{\Delta FIRE/\Delta FIRE}$ mice) do not have microglia throughout embryonic or postnatal life.[12,13] As *Csf1r*$^{\Delta FIRE/\Delta FIRE}$ mice reach adulthood, myelin abnormalities develop, but the mice are otherwise remarkably normal[14,15] and

Please cite this article in press as: Munro et al., Microglia protect against age-associated brain pathologies, Neuron (2024), https://doi.org/10.1016/j.neuron.2024.05.018

without the confounding impacts of CSF1R antagonists or homozygous *Csf1r* knockouts.[16,17] With aging, we provide evidence for the development of a neurodegenerative condition in $Csf1r^{\Delta FIRE/\Delta FIRE}$ mice with severe brain calcifications, disruptions in oligodendroglial gene expression, impairments in white matter integrity, and neuronal loss. Notably, each of these pathologies also occurs in human leukoencephalopathy patients carrying compound heterozygous or homozygous mutations in *CSF1R*.[18,19] In the accompanying study, Chadarevian and colleagues independently demonstrate many of these findings within humanized immune-deficient $Csf1r^{\Delta FIRE/\Delta FIRE}$ mice, further showing that microglial transplantation using CRISPR-corrected induced pluripotent stem cell (iPSC)-microglia-like cells can prevent and reverse these pathologies[1].

RESULTS

Non-microglial brain cells reach their mature transcriptomic states in the absence of microglia

Microglia are completely absent throughout $Csf1r^{\Delta FIRE/\Delta FIRE}$ brains during embryonic and postnatal life,[12,13] and we hypothesized that this would result in transcriptomic disturbances to other brain cell types. To map mRNA changes to specific brain cell types, we performed single-cell RNA sequencing (scRNA-seq) on live cells isolated from juvenile (6–7 weeks old) $Csf1r^{WT/WT}$, $Csf1r^{WT/\Delta FIRE}$, and $Csf1r^{\Delta FIRE/\Delta FIRE}$ brains. Cells were dissociated and sorted from both hippocampi and, separately, from the remainder of the left hemisphere after hippocampal dissection (Figures S1A and S1B). After quality control steps (see STAR Methods, Figures S1C–S1F, and Table S1), we examined the transcriptomes of 16,912 $Csf1r^{WT/WT}$, 15,133 $Csf1r^{WT/\Delta FIRE}$, and 15,493 $Csf1r^{\Delta FIRE/\Delta FIRE}$ brain cells. Expected brain cell populations were captured, but not at normal proportions: this dataset is glia-enriched due to our dissociation and sorting protocol (Figures 1A and S1G–S1I). Mature/myelinating oligodendrocytes from this dataset were recently subsetted and compared between $Csf1r^{WT/WT}$ and $Csf1r^{\Delta FIRE/\Delta FIRE}$ brains (see McNamara et al.[14]), but the remaining cell types have not yet been described. We provide an online resource to visualize transcriptomic changes in the different brain cell types in this dataset, as well as in the other datasets subsequently generated and described in this manuscript (link provided in the "data and code availability" section).

As clusters do not always capture continuous trajectories or provide a suitable resolution to understand cell state shifts, we performed "Milo" differential abundance testing.[21] Milo tests for significant abundance differences after assigning cells to small, partially overlapping cell "neighborhoods" on a k-nearest neighbor graph. Using this approach, we confirm the complete absence of microglia from $Csf1r^{\Delta FIRE/\Delta FIRE}$ brains (Figures 1B and 1C). Some border-associated macrophages (BAMs) were retained, but neighborhoods of these cells were significantly reduced in $Csf1r^{\Delta FIRE/\Delta FIRE}$ brains (Figures 1B and 1C), consistent with previous reports describing reduced macrophage densities in certain CNS border compartments[12,13] (Figures 1B and 1C). For the other brain cell types, Milo differential abundance testing revealed only very minor differences in cellular composition (Figures 1B and 1C), except from a previously described subpopulation of $Serpina3n^{high}C4b^{high}$ oligodendrocytes enriched in $Csf1r^{\Delta FIRE/\Delta FIRE}$ white matter.[14]

Although relative cell abundances were mostly similar in the different clusters, we wanted to determine whether cellular transcriptomic profiles differed between $Csf1r^{WT/WT}$ and $Csf1r^{\Delta FIRE/\Delta FIRE}$ brains by performing cluster-wise transcriptomic comparisons. We identified surprisingly few differentially expressed genes (DEGs) in the different brain cell clusters (using edgeR for pseudo-bulk transcriptomic comparisons and after removing predicted ambient RNAs, which are freely floating background transcripts captured alongside cells during the droplet-based encapsulation process; Figure 1D). The $Serpina3n^{high}C4b^{high}$ mOligo4 cluster was not included in Figure 1D as too few of these cells are present in $Csf1r^{WT/WT}$ brains to make the comparison (Figures S2A and S2B), but we previously subsetted and described these cells.[14] Of the other clusters analyzed, mOligo1-3 were the most transcriptionally different in $Csf1r^{\Delta FIRE/\Delta FIRE}$ brains, with enrichment of genes such as *Serpina3n, C4b*, *Cebpd*, and *Aldh2* indicating mild dysregulation of these cells. Other examples of DEGs in juvenile $Csf1r^{\Delta FIRE/\Delta FIRE}$ brain cells include upregulation of aldehyde dehydrogenase 7 family member A1 (*Aldh7a1*) in Astro1, oligodendrocyte precursor cells (OPCs), and iOligos, and upregulation of interferon alpha-inducible protein 27 (*Ifi27*) in OPC and iOligo clusters. Similar findings (i.e., minor transcriptional disruption of most cell types) were also observed after separating and analyzing cell clusters based on the tissue region from which they were obtained (Figures S2C and S2D), and when comparing cell clusters from heterozygous $Csf1r^{WT/\Delta FIRE}$ brains with the $Csf1r^{\Delta FIRE/\Delta FIRE}$ brain cells (Figure S2E; DEGs identified for the "iNeuron&iAstro" cluster likely reflect the different ratios of heterogeneous cell types in this small cluster being captured between genotypes).

As previous studies suggested roles for microglia in promoting oligodendrocyte maturation,[6,7,22–24] we next took advantage of capturing $Csf1r^{WT/WT}$ and $Csf1r^{\Delta FIRE/\Delta FIRE}$ oligodendrocytes across their developmental lineage by exploring their maturation trajectories (namely, OPCs, differentiation-committed oligodendrocyte precursors [COPs], newly forming oligodendrocytes, and mature/myelinating oligodendrocytes[20]; Figures 1E and 1F). Notably, the developmental profiles and trajectories of these cells during oligodendrogenesis were comparable in $Csf1r^{WT/WT}$ and $Csf1r^{\Delta FIRE/\Delta FIRE}$ brains (Figures 1G and 1H), indicating that microglia are dispensable for the normal transcriptomic maturation of oligodendrocytes in these mice. The finding that the other analyzed brain cell types also reached transcriptomic maturity in $Csf1r^{\Delta FIRE/\Delta FIRE}$ mice provides strong evidence that their mature profiles can also emerge independently from microglia (Figure 1D).

Together, these data indicate that the absence of microglia during embryonic and early postnatal life minimally impedes the transcriptomic maturation of other brain cell types. Moreover, we do not find evidence for a compensatory increase in the numbers of other macrophages/immune cell types during postnatal development when microglia are absent.

Microglial *Csf1r* haploinsufficiency has minor consequences on brain maturation

Reduced CSF1R levels due to lack of its production from one dysfunctional *CSF1R* allele (also known as *CSF1R* haploinsufficiency) has been claimed to be a cause of some cases of

Please cite this article in press as: Munro et al., Microglia protect against age-associated brain pathologies, Neuron (2024), https://doi.org/10.1016/j.neuron.2024.05.018

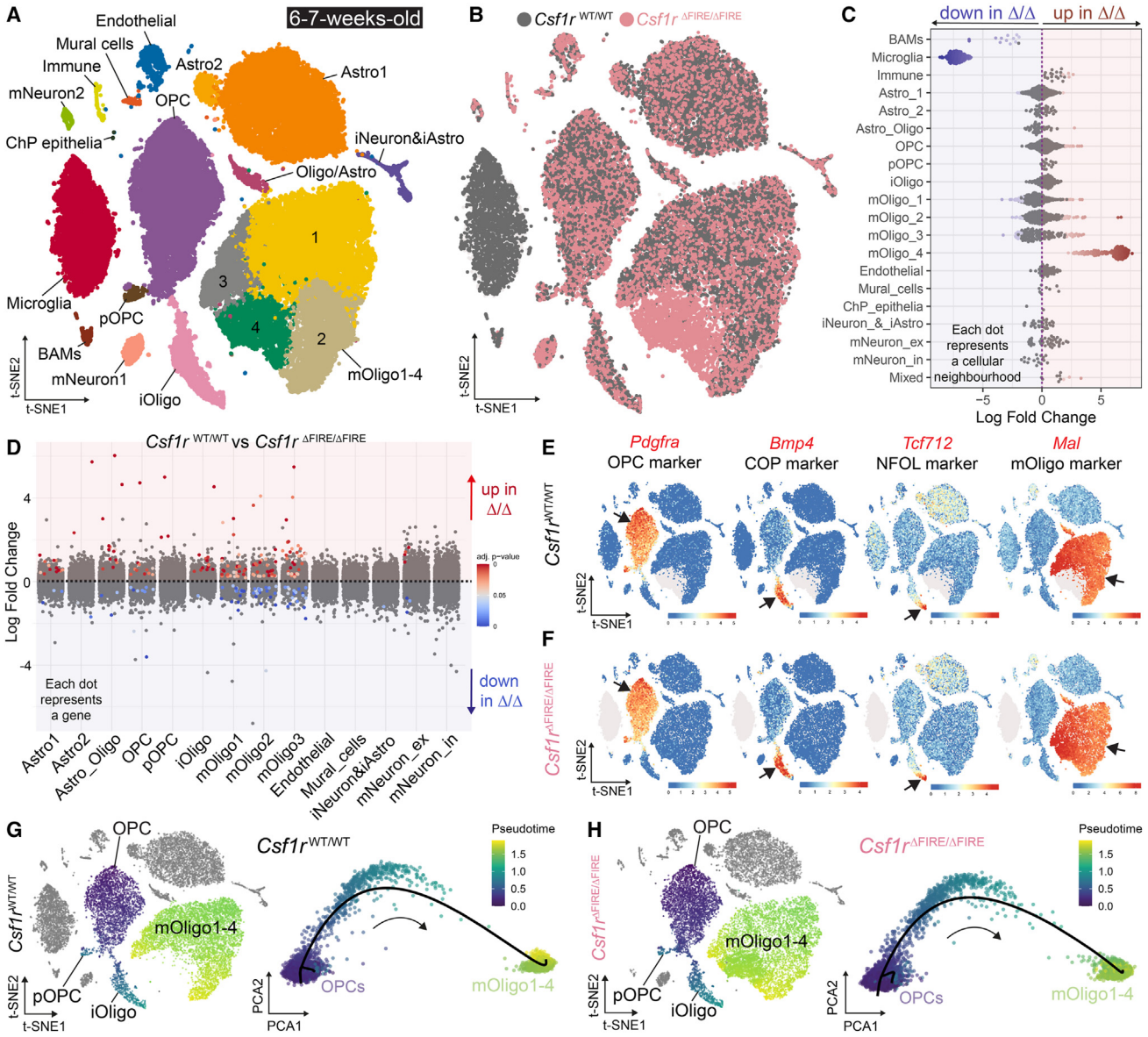

Figure 1. Sensitivities of different brain cell types to the absence of microglia in the juvenile brain

(A) Cells captured and analyzed for single-cell RNA sequencing from *Csf1r*$^{WT/WT}$ and *Csf1r*$^{\Delta FIRE/\Delta FIRE}$ brains (n = 4 samples per genotype from 2 *Csf1r*$^{WT/WT}$ mice and 2 *Csf1r*$^{\Delta FIRE/\Delta FIRE}$ mice, all females).

(B) Cell identities by genotype (gray cells from *Csf1r*$^{WT/WT}$ and pink cells from *Csf1r*$^{\Delta FIRE/\Delta FIRE}$ brains).

(C) Differential abundance comparison of cellular neighborhoods based on genotype (red dots = significantly increased abundance of cells in this neighborhood in *Csf1r*$^{\Delta FIRE/\Delta FIRE}$ brains; blue dots = significantly decreased abundance in *Csf1r*$^{\Delta FIRE/\Delta FIRE}$ brains; gray dots = not significantly altered).

(D) Differentially expressed genes (DEGs) for different cell clusters from *Csf1r*$^{WT/WT}$ and *Csf1r*$^{\Delta FIRE/\Delta FIRE}$ brains.

(E and F) Expression of different markers across the process of oligodendrogenesis in *Csf1r*$^{WT/WT}$ and *Csf1r*$^{\Delta FIRE/\Delta FIRE}$ brains. Pdgfra = OPCs; *Bmp4* = differentiation-committed oligodendrocyte progenitors (COPs); *Tcf7l2* = newly forming oligodendrocytes; *Mal* = mature/myelinating oligodendrocytes (markers based on Marques et al.[20]).

(G and H) Principal-component analysis (PCA) plots show trajectory analysis of (G) *Csf1r*$^{WT/WT}$ and (H) *Csf1r*$^{\Delta FIRE/\Delta FIRE}$ oligodendrocyte-lineage cells (differentiation trajectory/pseudotime goes from left to right, as indicated by arrows). t-distributed stochastic neighbor embedding (t-SNE) plots show the cells included in the oligodendrocyte trajectory analysis colored based on their pseudotime scores, and cells not included in this analysis shown in gray.

CSF1R-related leukoencephalopathy.[25,26] By contrast, other studies support a dominant-negative effect of disease-associated *CSF1R* mutations.[27,28] Regardless of the precise mechanism that underlies CSF1R-related leukoencephalopathy, the early life consequences of microglial *CSF1R* haploinsufficiency are incompletely understood.

Unlike mice with bi-allelic FIRE deletion, mice with single-allelic FIRE deletion (*Csf1r* $^{WT/\Delta FIRE}$ mice) retain both microglia

and BAMs.[12,13] However, we demonstrate that CSF1R (CD115) surface protein levels are approximately halved on microglia and other brain myeloid cells in *Csf1r*$^{WT/\Delta FIRE}$ brains compared with cells from control *Csf1r*$^{WT/WT}$ brains (Figures S3A–S3C). scRNA-seq substantiated this finding, as *Csf1r* mRNA levels were decreased in *Csf1r*$^{WT/\Delta FIRE}$ microglia (Figure S3D). These data reveal that FIRE deletion, even from just one allele, markedly alters *Csf1r*/CSF1R production by CNS macrophages (i.e., there is no dosage compensation from the wild-type allele), making this a useful model to study the consequences of microglial CSF1R haploinsufficiency.

In juvenile *Csf1r*$^{WT/\Delta FIRE}$ brains, the transcriptomic identities of haploinsufficient microglia were mildly disrupted (with 24 downregulated and 18 upregulated transcripts compared with *Csf1r*$^{WT/WT}$ microglia, based on adjusted $p < 0.05$), and we detected few differences in the abundances or transcriptomic profiles of other brain cell types compared with *Csf1r*$^{WT/WT}$ brain cells (Figures S3E–S3G). The developmental trajectory of oligodendrocyte-lineage cells (from OPCs to mature/myelinating oligodendrocytes) appeared normal in *Csf1r*$^{WT/\Delta FIRE}$ brains (Figures S3H and S3I), as was observed for the *Csf1r*$^{\Delta FIRE/\Delta FIRE}$ oligodendrocyte-lineage cells. Furthermore, we did not observe behavioral changes in the open-field test or elevated plus maze test between haploinsufficient *Csf1r*$^{WT/\Delta FIRE}$ and *Csf1r*$^{WT/WT}$ juvenile mice (for females or males; Figures S3J–S3M). These data indicate that there are only minor consequences of microglial *Csf1r* haploinsufficiency on brain cell status in juvenile mice.

Progressive glial cell disruption with aging in the absence of microglia

We have shown that many cell types in the juvenile mouse brain can develop with remarkably few transcriptomic alterations in the absence of microglia (Figure 1D). However, less is known about the consequences of permanent microglial deficiencies as the brain ages. We therefore examined cohorts of old *Csf1r*$^{WT/WT}$ and *Csf1r*$^{\Delta FIRE/\Delta FIRE}$ mice. We observed an age-associated decline in the well-being of *Csf1r*$^{\Delta FIRE/\Delta FIRE}$ mice, with 45% of *Csf1r*$^{\Delta FIRE/\Delta FIRE}$ mice reaching humane endpoints by 18 months of age (Figure 2A). Despite this, *Csf1r*$^{\Delta FIRE/\Delta FIRE}$ mice that survived to 15.5–17 months of age without apparent health issues did not exhibit clear signs of reduced activity or gait disturbances when compared with age-matched *Csf1r*$^{WT/WT}$ mice (Figures S4A–S4I). Nor did they exhibit differences in their hematological profiles at this age (Figures S4J–S4R). We also examined macrophage populations in peripheral organs of 15.5- to 17-month-old *Csf1r*$^{\Delta FIRE/\Delta FIRE}$ mice, finding the organs lacking or retaining resident macrophages were consistent with those previously described in juvenile *Csf1r*$^{\Delta FIRE/\Delta FIRE}$ mice[13] (Figure S5).

To examine whether brain cell profiles become increasingly dysregulated with aging in the absence of microglia, we performed scRNA-seq using 11- to 12-month-old brains (prior to apparent health issues in *Csf1r*$^{\Delta FIRE/\Delta FIRE}$ mice) and 16- to 18-month-old brains (when health issues are common in *Csf1r*$^{\Delta FIRE/\Delta FIRE}$ mice) (Figure 2A). Mixed single-cell suspensions were prepared from whole *Csf1r*$^{WT/WT}$ and *Csf1r*$^{\Delta FIRE/\Delta FIRE}$ brains using a similar protocol and approach as for Figure 1. Clusters from 11- to 12-month-old brains are labeled with a bold superscript "A" for adult (e.g., ^{A}Astro1), whereas clusters from 16- to 18-month-old brains are labeled with a bold superscript "O" for old (e.g., ^{O}Astro1) (Figures 2B and 2E).

As expected, microglia were still completely absent from *Csf1r*$^{\Delta FIRE/\Delta FIRE}$ brains at both 11–12 and 16–18 months of age (Figures 2B–2G). In 11- to 12-month-old *Csf1r*$^{\Delta FIRE/\Delta FIRE}$ brains, the proportions of other cell types were largely equivalent to those of their *Csf1r*$^{WT/WT}$ counterparts, although a small enrichment of certain non-microglial myeloid cells and lymphocytes was detected (Figures 2C and 2D). At 16–18 months of age, however, specific neighborhoods of OPCs and myelinating oligodendrocytes were highly enriched in *Csf1r*$^{\Delta FIRE/\Delta FIRE}$ brains, with 99% and 93% of cells in clusters ^{O}OPC2 and ^{O}mOligo2, respectively, being derived from *Csf1r*$^{\Delta FIRE/\Delta FIRE}$ samples (Figures 2E–2G). Abundances of captured vascular cells and astrocytes were largely unchanged at all ages examined (Figures 1C and 2C–2G).

We next performed differential expression analyses to explore the transcriptomic profiles of the captured brain cell types in adult (11–12 months old) and old (16–18 months old) mice. In 11- to 12-month-old mice, the transcriptomic profiles of most cell types were minimally disrupted in *Csf1r*$^{\Delta FIRE/\Delta FIRE}$ brains, except mature oligodendrocytes, which had upregulated markers previously described in "disease-associated" oligodendrocytes (DOLs), such as *Serpina3n* and *C4b*[29,30] (Figure 2H). In 16- to 18-month-old *Csf1r*$^{\Delta FIRE/\Delta FIRE}$ brains, transcriptomic dysregulation of astrocytes, OPCs, and mature oligodendrocytes was more striking, while we detected few DEGs for endothelia or mural cells at any age (the "mural cell" clusters in each dataset are predominantly comprised of pericytes; Figure 2I). Far fewer transcripts were altered at 11–12 months of age in *Csf1r*$^{\Delta FIRE/\Delta FIRE}$ OPCs, mature oligodendrocytes, and astrocytes when compared with 16–18 months of age. However, there was a high degree of overlap in the modified transcripts between both ages (Figure 3A), likely reflecting a progressive dysregulation of these cells with aging.

Astrocytes from 16- to 18-month-old *Csf1r*$^{\Delta FIRE/\Delta FIRE}$ brains had several upregulated transcripts previously associated with "pan-reactive astrocytes" (such as *Gfap*, *Vim*, *Aspg*, *Cd44*, and *Osmr*),[32] as well as mRNAs involved in cellular defense (e.g., *Aldh7a1*[33] and *Nrros*[34]) (Figure S6A). We identified the locations of reactive astrocytes *in situ* using glial fibrillary acidic protein (GFAP) immunofluorescence. GFAP^{high} astrocytes are enriched in the thalamus and the corpus callosum of 7- to 11-month-old and 18- to 19-month-old *Csf1r*$^{\Delta FIRE/\Delta FIRE}$ brains compared with age-matched *Csf1r*$^{WT/WT}$ brains (Figures 3B and 3C). In the older group of *Csf1r*$^{\Delta FIRE/\Delta FIRE}$ brains, abundant GFAP^{high} astrocytes were present throughout all observable white matter tracts (including the fimbria and internal capsule), whereas in the thalamus they were largely restricted to its ventral portion (Figure 3C). Numbers of GFAP^{high} astrocytes had also increased in the *Csf1r*$^{\Delta FIRE/\Delta FIRE}$ hippocampus and cortex by 18–19 months of age, but they did not differ in the hypothalamus at either age (Figure 3B).

Oligodendrocyte-lineage cells were also dysregulated in old *Csf1r*$^{\Delta FIRE/\Delta FIRE}$ brains. For the dysregulated cluster of mature oligodendrocytes enriched in 16- to 18-month-old *Csf1r*$^{\Delta FIRE/\Delta FIRE}$ brains (^{O}mOligo2), there were 1,741 upregulated and 1,072

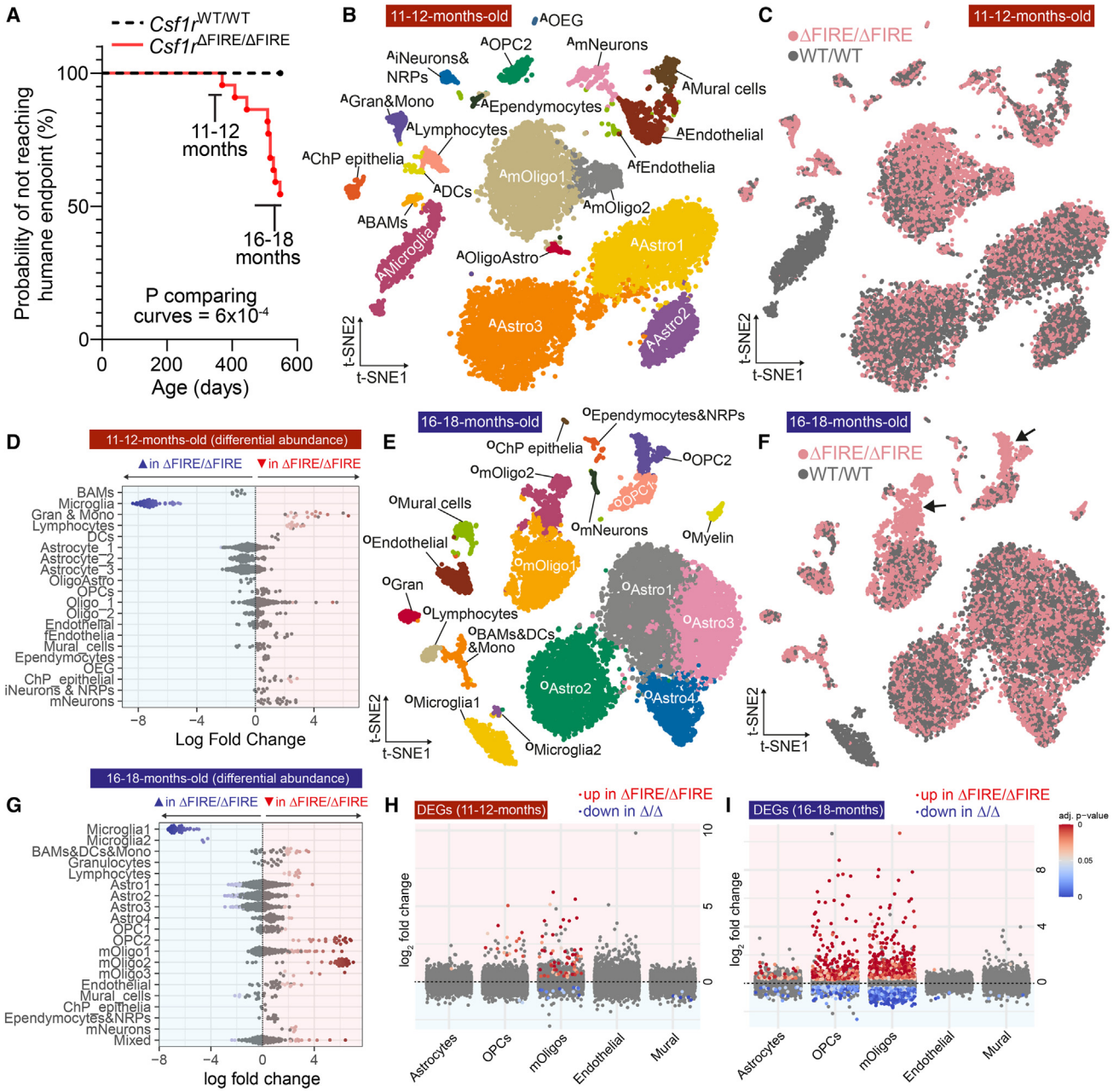

Figure 2. Increased glial cell disruption with aging in the absence of microglia

(A) Kaplan-Meier plot shows *Csf1r*$^{\Delta FIRE/\Delta FIRE}$ mice are more likely to reach humane endpoints with aging (n = 20 *Csf1r*$^{WT/WT}$ mice [8 females, 12 males], 22 *Csf1r*$^{\Delta FIRE/\Delta FIRE}$ mice [11 females, 11 males]; $p = 6 \times 10^{-4}$ using Mantel-Cox/log-rank test; chi-square = 11.65; df = 1). The ages used for single-cell RNA sequencing experiments are indicated.

(B–G) Single cells captured and sequenced from (B and C) 11- to 12-month-old and (E and F) 16- to 18-month-old *Csf1r*$^{WT/WT}$ and *Csf1r*$^{\Delta FIRE/\Delta FIRE}$ mice (n = 3 *Csf1r*$^{WT/WT}$ and 3 *Csf1r*$^{\Delta FIRE/\Delta FIRE}$ mice per age group, all males). (D and G) Milo differential abundance plots showing enriched and de-enriched neighborhoods of cells in (D) 11- to 12-month-old and (G) 16- to 18-month-old *Csf1r*$^{WT/WT}$ and *Csf1r*$^{\Delta FIRE/\Delta FIRE}$ mice. Arrows in (F) indicate the *Csf1r*$^{\Delta FIRE/\Delta FIRE}$ enriched clusters, ^{O}OPC2 and ^{O}mOligo2.

(H and I) Differential expression plots of main captured cell types in (H) 11- to 12-month-old and (I) 16- to 18-month-old *Csf1r*$^{WT/WT}$ and *Csf1r*$^{\Delta FIRE/\Delta FIRE}$ mice (gene colored only when significantly altered [red = upregulated; blue = downregulated], based on adjusted $p < 0.05$).

downregulated transcripts compared with cluster ^{O}mOligo1 (based on adjusted $p < 0.05$) (Figure S6B). Upregulated mRNAs include previously described DOL markers, such as *C4b* and *Serpina3n*,[30] and transcripts induced in oligodendrocytes during demyelination, such as *Syt4* and *Gdf15*.[35] Based on the DEGs in the ^{O}mOligo2 cluster, Ingenuity pathway analysis (IPA) predicted

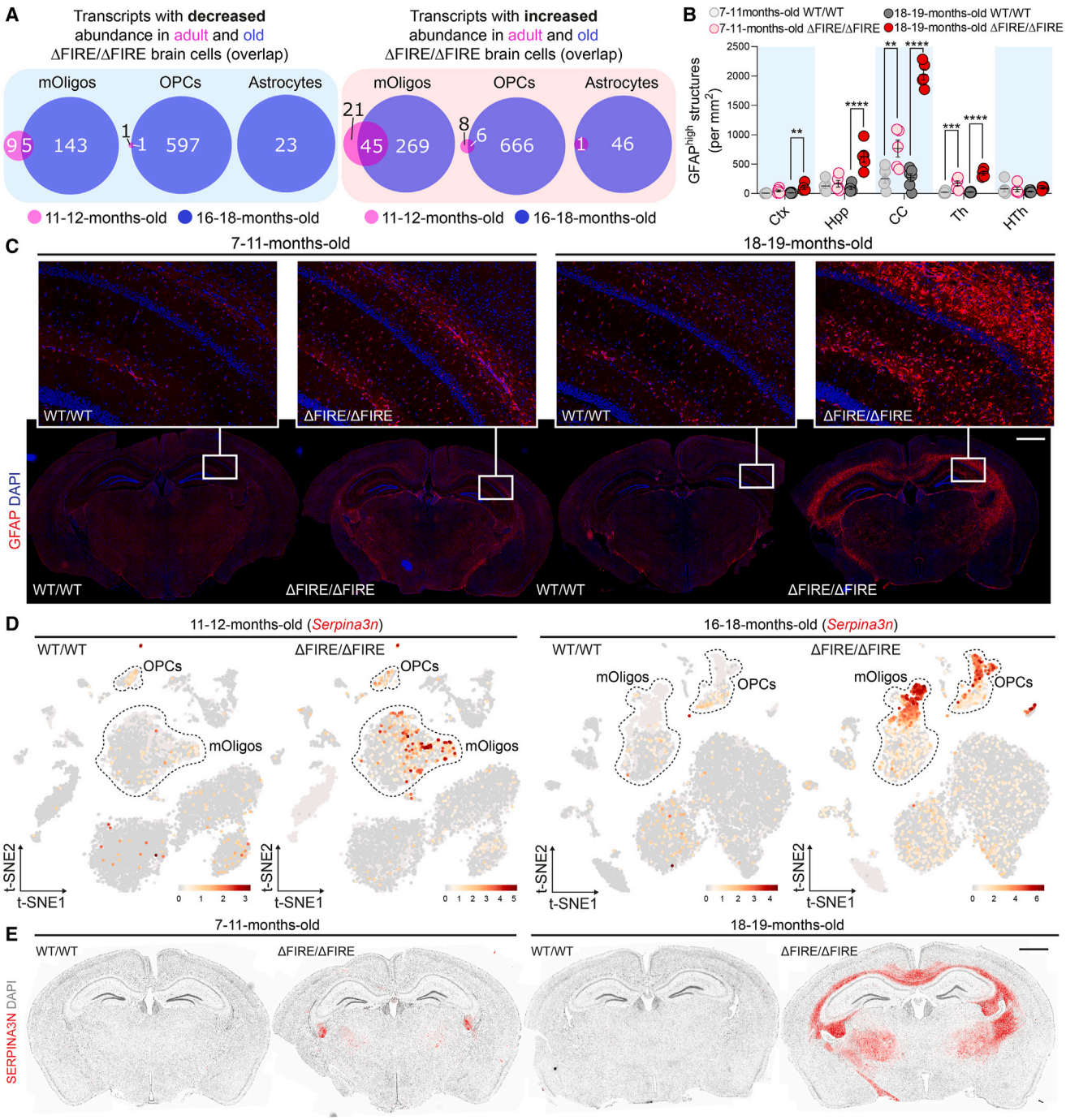

Figure 3. Macroglial dysregulation in the white matter and thalamus with aging in the absence of microglia

(A) Venn diagrams showing overlap of upregulated and downregulated transcripts in 11- to 12-months-old (lilac) and 16- to 18-months-old (blue) *Csf1r*$^{\Delta FIRE/\Delta FIRE}$ astrocytes, OPCs, and mature oligodendrocytes (based on adjusted $p < 0.05$). For illustrative purposes, Venn diagrams, which were created using DeepVenn,[31] are area proportional based only on the age group for a given cell type (not across cell types).

(B and C) Increased numbers of GFAP^{high} astrocytes with aging in the absence of microglia. Corpus callosal (CC), thalamic (Th), hippocampal (Hpp), and cortical (Ctx) GFAP^{high} astrocytes are increased in old brains. Hypothalamic (HTh) GFAP^{high} astrocyte numbers are not significantly altered (n = 5–6 mice per group [2–-3 females and 2–3 males per group]); groups compared by two-way ANOVA with Tukey's multiple comparison post hoc testing; ***$p < 0.001$, ****$p < 0.0001$; mean ± SEM shown for each group).

(legend continued on next page)

increased activation of several pathways, including those related to myelination (Z score = 2.33; $p = 7.25 \times 10^{-7}$), interferon signaling (Z score = 3; $p = 2.8 \times 10^{-6}$), and wound healing (Z score = 4; $p = 8.33 \times 10^{-10}$). WNT/β-catenin signaling, on the other hand, was predicted to be inhibited (Z score = −2.236; $p = 3.56 \times 10^{-6}$).

For the dysregulated cluster of aged *Csf1r*$^{\Delta FIRE/\Delta FIRE}$ OPCs (cluster ^{O}OPC2), there were 2,673 upregulated and 2,320 downregulated mRNAs compared with cluster ^{O}OPC1 (with adjusted $p < 0.05$) (Figure S6C). Based on the DEGs in the ^{O}OPC2 cluster, IPA predicted increased activation of eukaryotic initiation factor 2 (eIF2) signaling (Z score = 5.31; $p = 7.83 \times 10^{-39}$) and inhibition of both neurovascular coupling signaling (Z score = −4.44; $p = 4.95 \times 10^{-15}$) and synaptogenesis signaling (Z score = −4.26; $p = 1.5 \times 10^{-11}$). Some of the upregulated genes in ^{O}OPC2 were also increased in the dysregulated cluster of mOligos (^{O}mOligo2), such as *Serpina3n*, *C4b*, *Piezo2*, *Bmp4*, *Socs3*, and *Fos*; however, the dysregulation profiles of ^{O}OPC2s and ^{O}mOligo2s were largely distinct from each other (Figures S6D and S6E).

As expression of *Serpina3n*, a serine protease inhibitor, was massively enriched in clusters ^{O}OPC2 and ^{O}mOligo2 (Figure 3D), we investigated the location of these dysregulated cells *in situ* by performing immunohistochemistry for SERPINA3N and SOX10 (marking oligodendrocyte-lineage cell nuclei). SERPINA3N-immunoreactivity greatly increased with aging and was particularly high throughout the white matter and ventral thalamus of 16- to 18-month-old *Csf1r*$^{\Delta FIRE/\Delta FIRE}$ brains (Figure 3E). Notably, the distribution pattern of SERPINA3N changed with aging: in juvenile (6–7 weeks old) *Csf1r*$^{\Delta FIRE/\Delta FIRE}$ white matter, SERPINA3N signal was predominantly perinuclear (mostly abutting oligodendrocyte-lineage nuclei; Figure S6F), whereas puncta of SERPINA3N immunoreactivity in old *Csf1r*$^{\Delta FIRE/\Delta FIRE}$ brains were more widely distributed throughout the tissue (Figure S6G).

Next, to examine whether the effects of genotype on gene expression differ across ages (i.e., the genotype × age interaction), we integrated, re-clustered, and re-analyzed the 1- to 2-, 11- to 12-, and 16- to 18-month-old scRNA-seq datasets (Figures S7A and S7B). OPCs were by far the cell type with the most transcripts showing a significant genotype × age interaction, reflecting their dysregulation only in 16- to 18-month-old *Csf1r*$^{\Delta FIRE/\Delta FIRE}$ brains (example genes include *Sox11, Gap43*, and *Tmem176a*; Figure S7C; Table S2). Several mature oligodendrocyte transcripts also exhibited a significant genotype × age interaction, such as *Fxyd1* and *Cxcl14*, which are elevated with aging only in *Csf1r*$^{\Delta FIRE/\Delta FIRE}$ oligodendrocytes (Figures S7D–S7F). Few significant genotype × age interactions were found for transcripts in endothelia, mural cells, or astrocytes (for full results, see Table S2). Notably, re-analysis of all astrocytes after dataset integration shows that astrocyte subclusters 1 and 2, which transcriptomically resemble subcortical and gray matter astrocytes, respectively (e.g., *Agt* and *Nnat* enriched for subcortical, and *Igfbp2*, *Nupr1*, and *Il33* enriched for gray matter[36]), had more significantly altered transcripts than subcluster 3, which is enriched with white matter-associated transcripts (e.g., *Gfap*, *Tnc*, *Vim*, and *Thbs4* enriched[36]) (Figure S8; Table S3).

Taken together, these data reveal progressive dysregulation of macroglial cells with aging in the absence of microglia.

Atrophy, neuron loss, MRI hypointensities, and white matter deterioration in the microglia-deficient brain with aging

Based on our findings of localized cellular disruption with aging (particularly in the white matter and thalamus), we next sought to determine whether we could detect any corresponding regional abnormalities in the aging brain in the absence of microglia. To do so, we examined groups of adult (7–11 months old) and old (18–19 months old) *Csf1r*$^{WT/WT}$ and *Csf1r*$^{\Delta FIRE/\Delta FIRE}$ mouse brains using various MRI scanning protocols. Brains were scanned *ex vivo* within the cranial vault (to preserve morphology) using a 9.4T MRI scanner after immersion in a gadolinium-based contrast agent (Figure S9A).

We first performed region-wise volumetric quantifications by analyzing structural T2 scans using an image analysis pipeline that involved skull-stripping and image registration with a brain atlas (Figure 4A; Video S1). The average volume of *Csf1r*$^{\Delta FIRE/\Delta FIRE}$ brains was marginally increased at 7–11 months of age, but we found no differences in ventricular volume for either age group (relative to total brain volume; Figures S9B and S9C), despite ventriculomegaly being commonly reported in the literature in rodents and humans with *Csf1r/CSF1R* mutations that lead to a more global macrophage loss.[18,19,37] The relative volumes of the olfactory bulbs and hypothalami were decreased only in 7- to 11-month-old *Csf1r*$^{\Delta FIRE/\Delta FIRE}$ brains, albeit by a small amount (Figure S9C). The relative volumes of the thalamus, basal ganglia, and midbrain were subtly but significantly decreased only in 18- to 19-month-old *Csf1r*$^{\Delta FIRE/\Delta FIRE}$ brains (Figures 4B, 4C, and S9C).

White matter volume did not differ based on genotype (Figure 4D), but since we observed severe glial cell reactivity in white matter tracts (Figure 3), we next wanted to evaluate its structural integrity via diffusion-tensor magnetic resonance imaging (DTI). We reapplied the image registration used for the volumetric analysis to assess fractional anisotropy, mean diffusivity, radial diffusivity, and axial diffusivity across the volume of the white matter (by calculating a weighted mean score combining values from the corpus callosum, internal capsule, fimbria, and cerebellar white matter). These quantitative diffusivity metrics probe the relative diffusivity of water molecules along the different directions of fiber tracts and are commonly used to make inferences about white matter integrity. From this, we identified subtly but significantly reduced fractional anisotropy values (a measure of the directionality of diffusion anisotropy) for 7- to 11-month-old *Csf1r*$^{\Delta FIRE/\Delta FIRE}$ white matter compared with *Csf1r*$^{WT/WT}$ (values lower by 4.3% on average) and more strongly reduced fractional

(D) t-SNE plots showing *Serpina3n* mRNA levels in the different cell types captured at 11–12 and 16–18 months-old ($n = 3$ *Csf1r*$^{WT/WT}$ and 3 *Csf1r*$^{\Delta FIRE/\Delta FIRE}$ mice per age group).

(E) Immunohistochemistry shows increased SERPINA3N immunoreactivity in the white matter and thalamus of aged *Csf1r*$^{\Delta FIRE/\Delta FIRE}$ brains (images representative of 5–6 mice per group [2–3 females and 2–3 males per group]; colors inverted for illustrative purposes). Scale bars, 1 mm.

Please cite this article in press as: Munro et al., Microglia protect against age-associated brain pathologies, Neuron (2024), https://doi.org/10.1016/j.neuron.2024.05.018

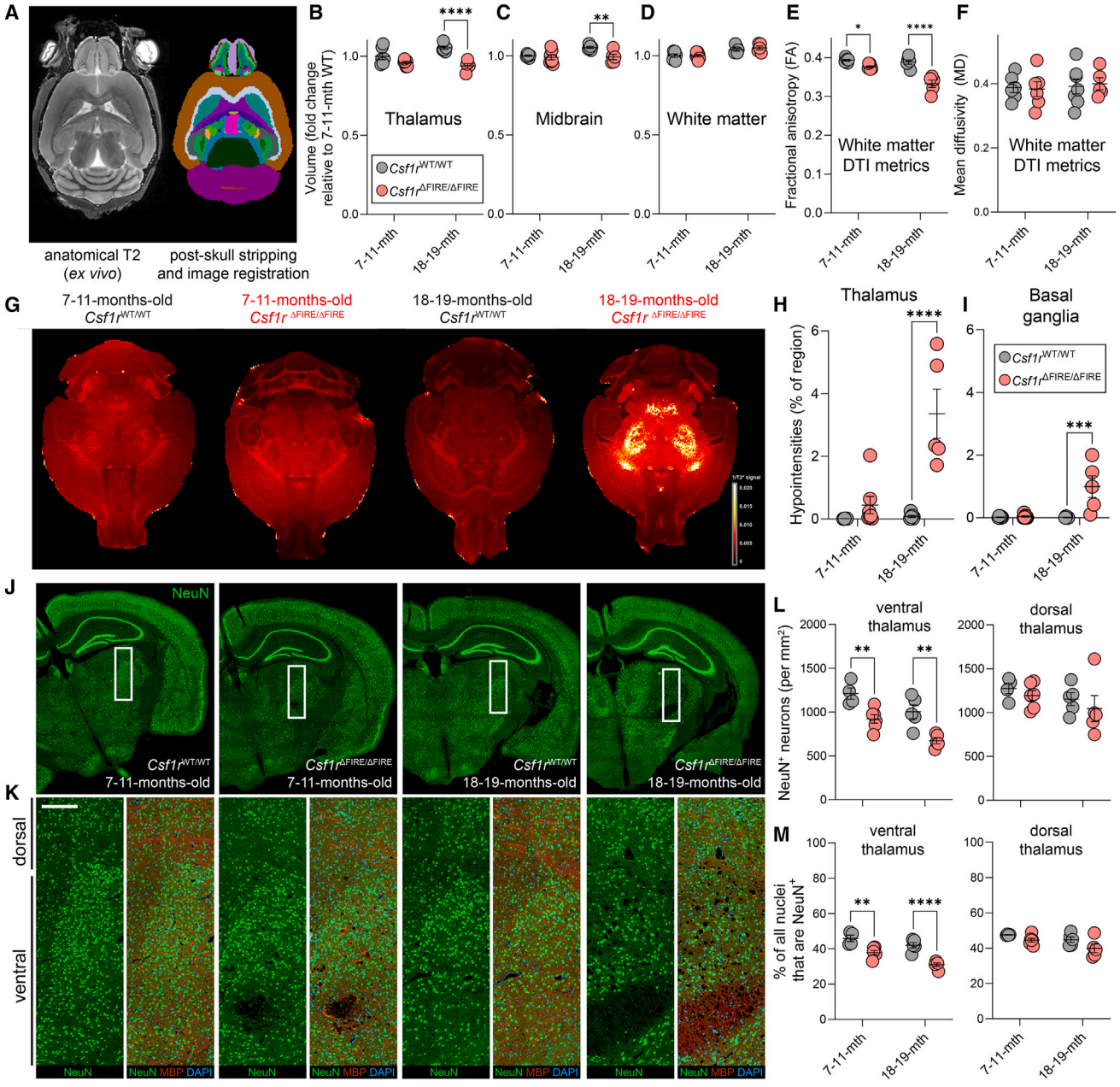

Figure 4. Regional atrophy, neuron loss, MRI hypointensities, and white-matter deterioration in the aging brain without microglia

(A) Example of a raw *ex vivo* MRI scan slice and a skull-stripped registered image used for analysis.

(B–D) Region-wise volumetric analysis of thalamus, midbrain, and white matter based on anatomical T2 scans (n = 5–7 mice per group [3 females and 2–4 males per group]; groups compared by two-way ANOVA with Tukey's multiple comparison post hoc testing; $^{**}p < 0.01$, $^{****}p < 0.0001$).

(E and F) Diffusion-tensor magnetic resonance imaging (DTI) values for fractional anisotropy and mean diffusivity (n = 5–7 mice per group; groups compared by two-way ANOVA with Tukey's multiple comparison post hoc testing; $^{*}p < 0.05$, $^{****}p < 0.0001$).

(G–I) Susceptibility-weighted imaging MRIs show regional hypointensities in *Csf1r*$^{\Delta FIRE/\Delta FIRE}$ mice (hypointensities pseudo-colored based on intensity; n = 5–7 mice per group [3 females and 2–4 males per group]; groups compared by two-way ANOVA with Tukey's multiple comparison post hoc testing; $^{***}p < 0.001$, $^{****}p < 0.0001$).

(J and K) Immunohistochemistry for neuronal nuclear antigen (NeuN) and myelin basic protein (MBP) with DAPI labeling of *Csf1r*$^{WT/WT}$ and *Csf1r*$^{\Delta FIRE/\Delta FIRE}$ brain sections (region shown in K corresponds to the area within the rectangular box in J).

(L and M) Quantifications of neuronal numbers (per mm^2) and the percentage of cells that are neurons show fewer neurons in the *Csf1r*$^{\Delta FIRE/\Delta FIRE}$ ventral thalamus at 7–11 and 18–19 months (n = 4–6 mice per group [2–3 females and 2–3 males per group]; groups compared by two-way ANOVA with Tukey's multiple comparison post hoc testing$^{**}p < 0.01$, $^{****}p < 0.0001$). Mean ± SEM shown for plotted data. Scale bars, 200 μm.

anisotropy values for 18- to 19-month-old *Csf1r*$^{\Delta FIRE/\Delta FIRE}$ white matter (values lower by 14.4% on average) (Figure 4E), suggesting worsening white matter condition with aging (two-way ANOVA interaction $p = 0.001$; full two-way ANOVA tables can be found in Table S4). Other DTI metric values (i.e., axial, radial, and mean diffusivity) did not significantly differ between genotypes (Figures 4F, S9D, and S9E).

Next, our findings of mild regional atrophy led us to examine brains for further abnormalities using 3D high-spatial-resolution susceptibility-weighted imaging (SWI) MRI. SWI sequences are particularly sensitive to compounds that distort the magnetic field (appearing as dark, hypointense signals in scans), such as blood products, iron, and calcium, which can be difficult to identify using other MRI sequences.[38] Using SWI, we identified several brain regions with significantly more hypointensities in the 18- to 19-month-old *Csf1r*$^{\Delta FIRE/\Delta FIRE}$ group (namely, the thalamus, basal ganglia, and pons; Figures 4G–4I and S9F; Video S2). The tissue volume covered by hypointensities in other brain regions, such as the white matter and hippocampus, did not differ based on genotype (Figures S9G and S9H).

Based on the atrophy, MRI hypointensities, and glial cell reactivity observed in the aging *Csf1r*$^{\Delta FIRE/\Delta FIRE}$ thalamus, we next examined whether neuronal phenotypes were also altered in this region. The fixed brains used for MRIs were dissected from their cranial vaults, and coronal sections were cut to the appropriate depth for processing. Anti-NeuN immunohistochemistry demonstrated that the number of neurons per area, as well as the proportion of cells that were neuronal, were reduced in the *Csf1r*$^{\Delta FIRE/\Delta FIRE}$ thalamus (Figures 4J, S9I, and S9J). Notably, the ventral portion of the aging *Csf1r*$^{\Delta FIRE/\Delta FIRE}$ thalamus had a particularly low number (per area) and proportion of neurons (Figures 4K–4M). The number of NeuN^{+} neurons per area and the proportion of neurons did not significantly differ in other brain regions examined, except in the cortex of 7- to 11-month-old *Csf1r*$^{\Delta FIRE/\Delta FIRE}$ mice (compared with age-matched *Csf1r*$^{WT/WT}$ controls; Figures S9I and S9J).

Together, these data show highly selective regional atrophy, MRI hypointensities, neuron loss, and white matter deterioration with aging in the absence of microglia. These anatomical and cellular defects spatiotemporally correspond to the brain regions with the most striking macroglial reactivity (i.e., the white matter and thalamus; Figure 3).

Thalamic calcification is massively accelerated and intensified with aging in the absence of microglia

To identify the source(s) of the hypointensities observed in Figure 4G, we stained coronal sections with various histostains at the depth of the thalamus, where hypointensities appeared most severe. We show that thalamic regions in *Csf1r*$^{\Delta FIRE/\Delta FIRE}$ groups show marked calcium deposition, as evidenced by staining for alizarin red and von Kossa (Figures 5A, 5B, and S10A). We did not see positive staining for iron (Prussian blue) or amyloid fibrils (Congo red) on sections examined containing calcified thalamic regions (Figures S10B and S10C). Thalamic calcifications often centered on ventral posteromedial and ventral posterolateral nuclei, while dorsal lateral regions of the thalamus were relatively preserved (Figure S11). Calcifications were already present in the 7- to 11-month-old *Csf1r*$^{\Delta FIRE/\Delta FIRE}$ group but progressively worsened with aging (two-way ANOVA interaction $p < 0.0001$; Figures 5A and 5B). Thalamic calcifications also immunostained for the bone-matrix protein, osteopontin (SPP1), and we found that GFAP^{high} astrocytes encircled these SPP1^{+} structures in 18- to 19-month-old *Csf1r*$^{\Delta FIRE/\Delta FIRE}$ brains (Figure 5C).

The thalamus is particularly prone to ectopic calcifications in the mouse brain, as shown in normal aging[39–42] and in several genetically modified mouse lines.[43–46] A suggested mechanism by which brain calcifications may form is due to phenotypic changes of resident brain cells (such as astrocytes, endothelial cells, and pericytes) toward an osteoblast-like/pro-mineralization state.[47] To assess whether any resident brain cells change phenotype in a manner that may promote calcification deposition in *Csf1r*$^{\Delta FIRE/\Delta FIRE}$ brains, we explored thalamic cell profiles using scRNA-seq. Cell clusters from this dataset are labeled with a bold superscript "TH" for thalamus (e.g., THAstro1) (Figure 5D).

Microglia were completely absent from 17- to 19-month-old *Csf1r*$^{\Delta FIRE/\Delta FIRE}$ thalami, whereas some cellular neighborhoods of OPCs and mature oligodendrocytes were over-represented compared with control mice (Figure 5E). Transcriptomic profiles of captured thalamic *Csf1r*$^{\Delta FIRE/\Delta FIRE}$ endothelia and mural cells were largely unchanged (Figure 5F). By contrast, thalamic *Csf1r*$^{\Delta FIRE/\Delta FIRE}$ astrocytes, OPCs, and mature oligodendrocytes were enriched for previously described CNS injury/disease-associated markers (such as *Gfap*, *Stat3*, and *Egr1* for astrocytes; *Slc14a1* and *Mylk* for OPCs; and *Serpina3n*, *C4b*, and *Tnfrsf1a* for mature oligodendrocytes)[29,30,32,48,49] (Figure 5F). Within the thalamus, immunohistochemical staining demonstrated that GFAP^{high} astrocytes and SERPINA3N puncta were particularly abundant in calcified regions (Figures 5C and S12A).

We did not observe differential expression of mRNAs previously linked to calcification formation/osteogenic states (such as *Bglap*, *Ibsp*, *Sp7*, *Alpl*, *Spp1*, and *Runx2*) in any cell type. Rather, IPA predicted pathway activation related to osteoclasts (bone-clearing cells) in *Csf1r*$^{\Delta FIRE/\Delta FIRE}$ OPCs and mature oligodendrocytes (Figures S12B and S12C). Interferon signaling was also predicted to be activated in *Csf1r*$^{\Delta FIRE/\Delta FIRE}$ oligodendrocytes, whereas cell cycle pathways were predicted to be activated in *Csf1r*$^{\Delta FIRE/\Delta FIRE}$ OPCs (Figures S12D and S12E). Indeed, there were consistently more marker of proliferation Kiel 67 (*mKi67*)$^{+}$ OPCs in *Csf1r*$^{\Delta FIRE/\Delta FIRE}$ thalami compared with in *Csf1r*$^{WT/WT}$ thalami (Figure S12F). Few pathways were predicted to be activated or inactivated in *Csf1r*$^{\Delta FIRE/\Delta FIRE}$ astrocytes, perhaps owing to the small number of DEGs identified for this cell type.

As the thalamus is prone to calcification formation with aging,[39,42] we reasoned that we may also be able to observe these structures forming in the thalamus of aging wild-type mice. Using immunohistochemistry, we detected a few sporadic SPP1^{+} structures, which were enwrapped by GFAP^{+} astrocytes, in the ventral thalamus of 18- to 19-month-old *Csf1r*$^{WT/WT}$ mice (Figure S13A). Thalamic microglia were also intimately associated with these SPP1^{+} structures in *Csf1r*$^{WT/WT}$ brains (Figures 5G and 5H). We next mined our thalamic scRNA-seq dataset to identify cellular sources of *Spp1* in *Csf1r*$^{WT/WT}$ and *Csf1r*$^{\Delta FIRE/\Delta FIRE}$ brains. Most *Spp1*-expressing cells in *Csf1r*$^{\Delta FIRE/\Delta FIRE}$ thalami were in clusters of non-microglial myeloid cells and in a small cluster of perivascular fibroblasts[50]

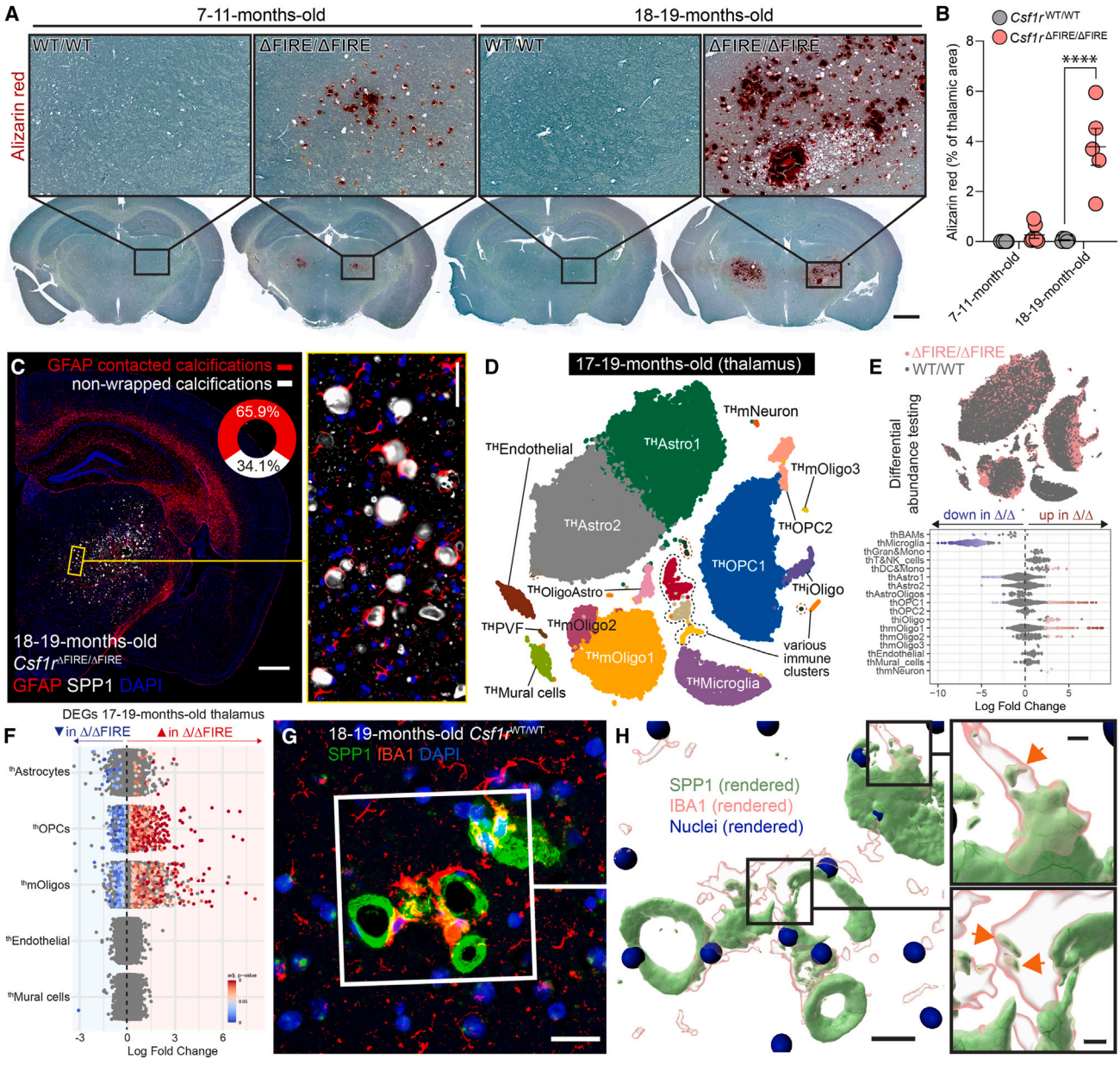

Figure 5. Severe bilateral calcifications and glial cell disruption in the aging *Csf1r*$^{\Delta FIRE/\Delta FIRE}$ thalamus

(A and B) Alizarin red staining shows calcifications in *Csf1r*$^{\Delta FIRE/\Delta FIRE}$ brains, which are particularly severe in the ventral thalamus and progressively worsen with aging (n = 5–7 mice per group [3 females and 2–4 males per group]; groups compared by two-way ANOVA with Šidák's multiple comparison post hoc testing; ****$p < 0.0001$. Two-way ANOVA interaction $p < 0.0001$; mean ± SEM shown for each group).

(C) Calcifications are immunoreactive for SPP1 and are frequently surrounded by GFAP^{high} astrocytes (65.9% ± 1.7% SEM of thalamic SPP1^{+} structures are in contact with GFAP^{high} astrocytes; n = 3 mice [1 female, 2 males], values averaged from 3 regions of interest per mouse).

(D) Cells captured and analyzed for single-cell RNA sequencing from 17- to 19-month-old *Csf1r*$^{WT/WT}$ and *Csf1r*$^{\Delta FIRE/\Delta FIRE}$ thalami (n = 27,345 cells from 4 *Csf1r*$^{WT/WT}$ [3 females, 1 male] and 21,788 cells from 4 *Csf1r*$^{\Delta FIRE/\Delta FIRE}$ mice [1 female, 3 males]). Cells outlined with brown dashed lines are part of the THMixed cluster.

(E) Differential abundance comparison of cellular neighborhoods based on genotype (red dots = significantly increased abundance of cells in this neighborhood in *Csf1r*$^{\Delta FIRE/\Delta FIRE}$ thalami; blue dots = significantly decreased abundance in *Csf1r*$^{\Delta FIRE/\Delta FIRE}$ thalami; gray dots = not significantly altered).

(F) Differential expression plots for main captured cell types.

(G) Z-projection of an immunohistochemical image showing SPP1^{+} structures enwrapped by IBA1^{+} microglia in the thalamus of a 17- to 19-month-old *Csf1r*$^{WT/WT}$ brain.

(H) Volume rendered image created in IMARIS based on signal from SPP1 (green), IBA1 (red, transparent), and DAPI (blue). The region shown corresponds to the area highlighted by the white box in (G). Inset boxes show SPP1^{+} structures within the cytoplasm of microglia. Scale bars: 1 mm for (A); 500 μm for (C) (inset box = 50 μm); 20 μm for (G); 10 μm for (H) (inset boxes = 2 μm).

(Figure S13B). The same cellular sources of *Spp1* were present in the *Csf1r*$^{WT/WT}$ thalamus, with the addition of microglia as an *Spp1* source in these brains (Figure S13B).

These data show that ectopic calcification with aging is dramatically accelerated in the absence of microglia. Non-microglial thalamic *Csf1r*$^{\Delta FIRE/\Delta FIRE}$ glial cells display reactive phenotypes, but they appear not to shift toward an osteoblast-like/pro-mineralizing state.

Vascular alterations in severely calcified regions of the *Csf1r*$^{\Delta FIRE/\Delta FIRE}$ thalamus

The thalamus is a densely vascularized brain region that is vulnerable to vascular damage with aging, and vascular dysfunction is a suggested route by which thalamic calcifications may form.[47,51,52] We therefore analyzed the thalamic vasculature in 6- to 11-month-old *Csf1r*$^{WT/WT}$ and *Csf1r*$^{\Delta FIRE/\Delta FIRE}$ mice. At this age, *Csf1r*$^{\Delta FIRE/\Delta FIRE}$ brains show incipient thalamic calcification, which has not yet expanded extensively (Figure 5A). To assess the microanatomical localization of calcifications within *Csf1r*$^{\Delta FIRE/\Delta FIRE}$ thalami, we co-immunostained free-floating sections for SPP1 and an astrocyte end-feet marker, β-dystroglycan. We confirmed that SPP1$^+$ demarcates the boundaries of calcified structures using two fluorescently labeled bisphosphonates, zoledronate and risedronate, which bind hydroxyapatite crystals[53] (Figures 6A and 6B). Volume rendering of confocal z-stacks demonstrated that some SPP1$^+$ structures were in contact with the vasculature (45% ± 3.8% SEM), while others were parenchymal (Figures 6C and 6D). Vessel-associated SPP1$^+$ structures varied greatly in size and were occasionally almost entirely intravascular (Figures S14A and S14B). We also show that thalamic calcifications label positively for amyloid precursor protein (APP) and/or osteocalcin, proteins detected in calcifications in other neurodegenerative diseases[47] (Figure S14C). These data indicate that thalamic calcifications are heterogeneous in terms of both their microenvironments and features in *Csf1r*$^{\Delta FIRE/\Delta FIRE}$ brains.

As many calcifications associate with the vasculature in thalami of *Csf1r*$^{\Delta FIRE/\Delta FIRE}$ mice, we next assessed whether blood flow and/or vascular status are altered in this brain region of *Csf1r*$^{\Delta FIRE/\Delta FIRE}$ mice. To quantify thalamic blood flow *in vivo* in 8- to 11-month-old mice, we performed arterial spin labeling (ASL) MRIs after identifying the correct scanning depth using *in vivo* coronal T2-scans to localize calcifications (Figure 6E). Notably, the thalamus was the most highly perfused brain region examined in both *Csf1r*$^{WT/WT}$ and *Csf1r*$^{\Delta FIRE/\Delta FIRE}$ mice, but we did not identify genotype-based blood flow differences in any region (Figure 6F).

Next, to examine the status of the thalamic vasculature, we co-immunolabeled free-floating sections with anti-CD31 (which labels endothelia), anti-ERG (which labels endothelial nuclei), and anti-CD13 (which labels pericytes), followed by spinning disk confocal imaging (Figure 6G). We identified no differences in vascular density in the dorsal or ventral thalamus of 8- to 11-month-old *Csf1r*$^{\Delta FIRE/\Delta FIRE}$ mice compared with *Csf1r*$^{WT/WT}$ mice (Figure 6H). However, pericyte coverage of the vasculature was subtly decreased throughout the *Csf1r*$^{\Delta FIRE/\Delta FIRE}$ thalamus across a range of vessel diameters (Figures 6I and 6J). We also observed a small corresponding increase in average blood vessel diameter in the ventral thalamus (Figure 6K).

A recent study in a mouse model of dominantly inherited primary familiar brain calcification (PFBC) suggested that astrocytes in the vicinity of vascular calcifications exhibit increased reactivity and reduced end-feet coverage of the cerebral vasculature.[54] Consistent with this report, we observed increased GFAP levels (Figures 3B and 5C) and a mis-localization of the astrocytic end-feet markers, aquaporin 4 and β-dystroglycan, from some blood vessels in heavily calcified regions of the *Csf1r*$^{\Delta FIRE/\Delta FIRE}$ ventral thalamus (Figures S14D and S14E). Reduced end-feet coverage and reduced pericyte coverage of vessels often coincides with blood-brain barrier (BBB) breaches, but we did not find evidence for increased fibrinogen deposition, a marker indicating a leaky BBB, in the thalamus of *Csf1r*$^{\Delta FIRE/\Delta FIRE}$ mice or elsewhere in the brain (Figure S14F). Nor did we identify differences in endothelial, mural cell, or astrocytic expression of transcripts linked to BBB maintenance (Figures S14G–S14I).

Populating *Csf1r*$^{\Delta FIRE/\Delta FIRE}$ brains with wild-type microglia prevents pathology development

To verify that microglia provide resilience against brain calcification, we populated the empty parenchymal niche of postnatal day (P)1 *Csf1r*$^{\Delta FIRE/\Delta FIRE}$ brains with donor wild-type microglia, using a previously validated approach.[55] A total of 50,000 P2 wild-type C57BL/6 primary mouse microglia were injected into the brain of each pup. Groups of microglia-injected and PBS-injected *Csf1r*$^{\Delta FIRE/\Delta FIRE}$ mice were then aged to 9 months of age, a time point at which thalamic calcifications have started forming in the absence of microglia. Microglial transplantations resulted in brain-wide engraftment and the population of the empty microglial niche in *Csf1r*$^{\Delta FIRE/\Delta FIRE}$ brains (Figures 7A and 7B). Through these microglial injections, we prevented thalamic calcification formation in 9-month-old *Csf1r*$^{\Delta FIRE/\Delta FIRE}$ brains, as shown via staining with both alizarin red (Figures 7C and 7D) and risedronate-647 (Figure S15). We also show reduced astrocyte reactivity and increased neuronal numbers in the thalami of microglia-injected *Csf1r*$^{\Delta FIRE/\Delta FIRE}$ brains compared with PBS-injected controls (Figures 7E and 7F).

Besides the thalamic pathologies, oligodendrocytes with "disease-associated" profiles[29,30] reside within white matter tracts of microglia-deficient *Csf1r*$^{\Delta FIRE/\Delta FIRE}$ brains, and axonal spheroids are also present.[1,14] We next assessed whether microglia-transplanted *Csf1r*$^{\Delta FIRE/\Delta FIRE}$ brains are also protected from these phenotypes. For DOLs, we immunolabeled sections for anti-SERPINA3N, showing its levels are strongly reduced in the fimbriae of microglia-injected *Csf1r*$^{\Delta FIRE/\Delta FIRE}$ brains compared with age-matched PBS-injected *Csf1r*$^{\Delta FIRE/\Delta FIRE}$ brains, whereas the numbers of OLIG2$^+$ oligodendrocytes do not differ (Figures 7G and 7H). To examine axonal spheroids, characteristic features of adult-onset leukoencephalopathy with axonal spheroids and pigmented glia (ALSP) cases,[56] we stained sections for anti-SMI312, which labels phosphorylated axonal epitopes of neurofilaments.[57] As expected, many SMI312$^+$ axonal spheroids were present in control *Csf1r*$^{\Delta FIRE/\Delta FIRE}$ brains, whereas very few were present in age-matched microglia-injected *Csf1r*$^{\Delta FIRE/\Delta FIRE}$ brains (Figure 7I).

These data show that populating the *Csf1r*$^{\Delta FIRE/\Delta FIRE}$ brain with donor wild-type microglia from early in postnatal life protects against the subsequent development of various age-associated brain pathologies.

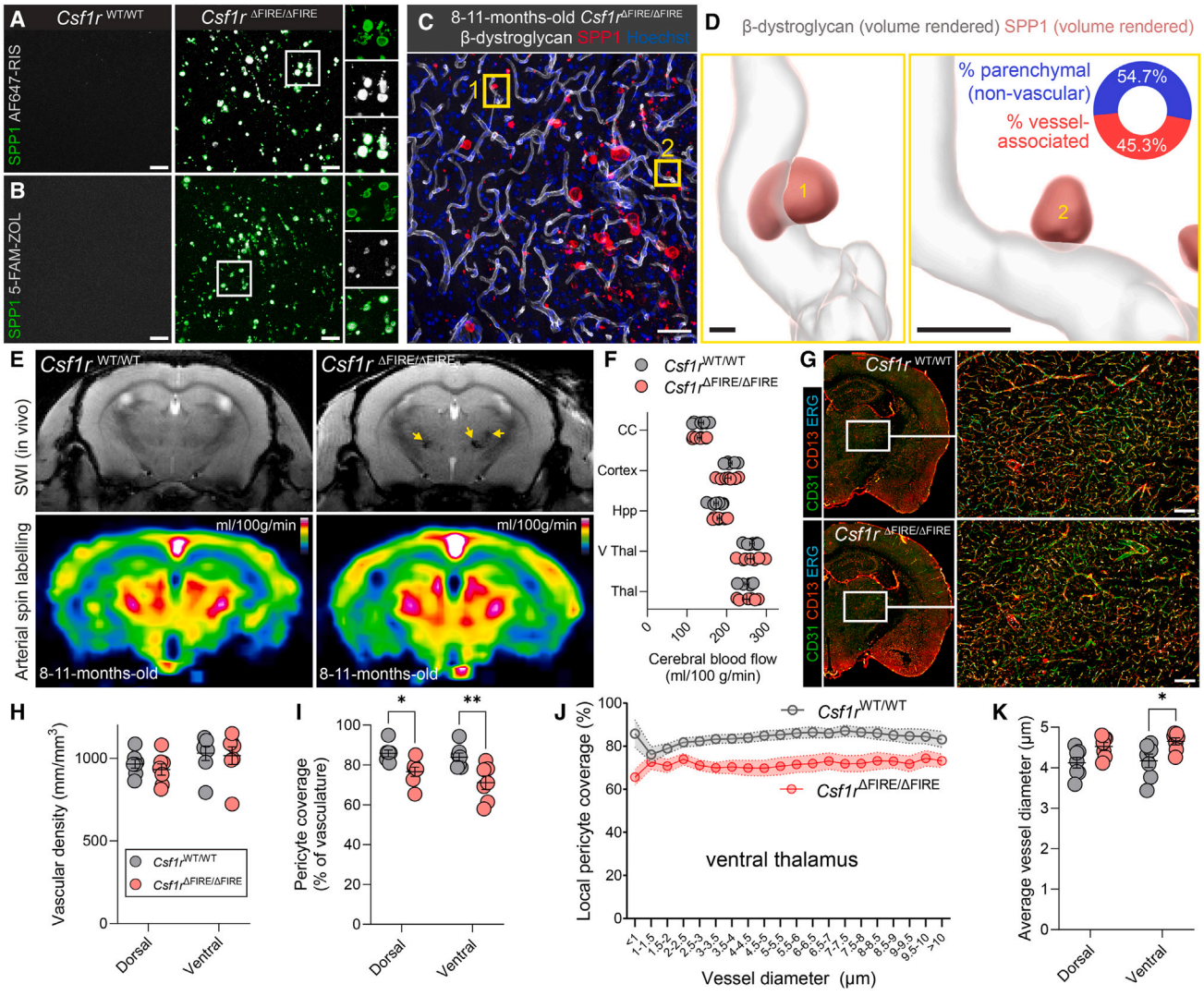

Figure 6. Mild vascular disruption in heavily calcified thalamic regions

(A and B) SPP1^{+} demarcates the boundaries of calcified structures, as shown by co-labeling with two fluorescently modified bisphosphonates, zoledronate (5-FAM-ZOL) and risedronate (AF647-RIS).

(C and D) Immunohistochemistry for SPP1 and β-dystroglycan shows that capillary calcifications are common in the thalami of 8- to 11-month-old *Csf1r*$^{\Delta FIRE/\Delta FIRE}$ mice (45% ± 3.8% SEM of thalamic SPP1^{+} structures are in contact with blood vessels; $n = 7$ male *Csf1r*$^{\Delta FIRE/\Delta FIRE}$ mice). Images in (D) volume rendered from the yellow boxed regions in (B).

(E and F) Arterial spin labeling (ASL) MRIs indicate no differences in cerebral blood flow *in vivo* in 8- to 11-month-old *Csf1r*$^{\Delta FIRE/\Delta FIRE}$ brains compared with age-matched *Csf1r*$^{WT/WT}$ brains ($n = 7$ mice per group [all males]; groups compared by two-way ANOVA). ASL images in (E) were smoothed for illustrative purposes using median filtering in ImageJ. CC, corpus callosum; Hpp, hippocampus; V Thal, ventral thalamus. SWI scans in (E) confirm calcifications had already started forming in *Csf1r*$^{\Delta FIRE/\Delta FIRE}$ thalami at the ASL scanning depth.

(G) Immunohistochemistry for CD31, CD13, and ETS-related gene (ERG; marking endothelial nuclei) in thick free-floating brain sections from 8- to 11-month-old *Csf1r*$^{WT/WT}$ and *Csf1r*$^{\Delta FIRE/\Delta FIRE}$ mice (images representative of $n = 7$ mice per group [all males]).

(H–K) Quantification of (H) vascular density, (I and J) pericyte coverage, and (K) vessel diameters in the dorsal and ventral thalamus (through analysis of stitched spinning disk confocal microscopy images shown in G; $n = 7$ mice per group [all males]; groups compared by two-way ANOVA with Šidák's multiple comparison post hoc testing; $^{*}p < 0.05$, $^{**}p < 0.01$). Mean ± SEM shown for plotted data. Scale bars: 50 μm for (C); 5 μm for (D) (left image) and 10 μm for (D) (right image); 100 μm for (G).

DISCUSSION

Many non-immune functions have been assigned to microglia in development and adulthood.[2] Here, we found no compelling evidence that microglia are required for the maturation of other brain cell types. Rather, using diverse tools, our data suggest that microglia provide resilience against detrimental brain changes with aging. Our findings thus highlight important new functions of microglia with important implications for the pathogenesis of neurodegenerative diseases and the development of CSF1R-related leukoencephalopathies.

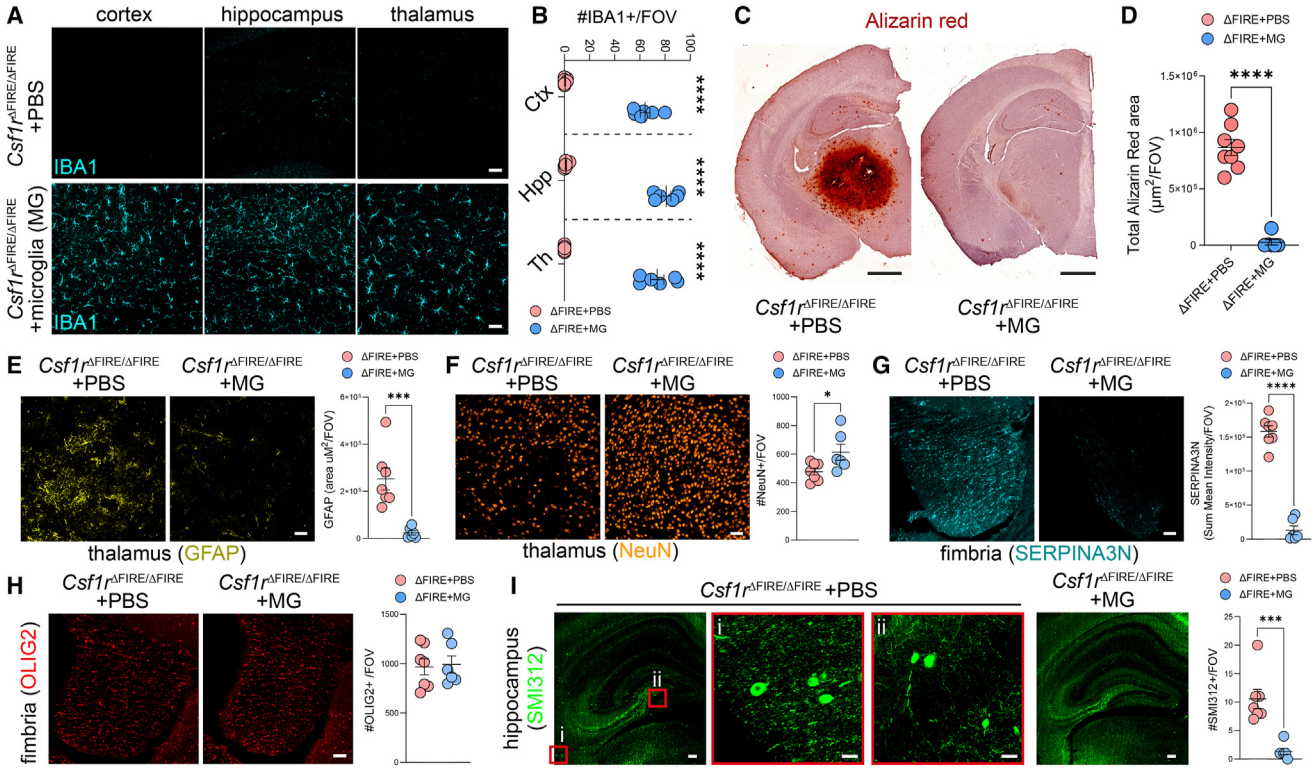

Figure 7. Populating *Csf1r*$^{\Delta FIRE/\Delta FIRE}$ brains with wild-type microglia protects against the development of diverse pathologies

(A and B) Transplantation of wild-type donor microglia at P1 results in brain-wide microglial engraftment, as shown in 9 months of age *Csf1r*$^{\Delta FIRE/\Delta FIRE}$ brains. CTX, cortex; Hpp, hippocampus; Th, thalamus; MG, microglia.

(C and D) Microglia-injected *Csf1r*$^{\Delta FIRE/\Delta FIRE}$ brains are protected against calcification development at 9 months of age compared with PBS-injected *Csf1r*$^{\Delta FIRE/\Delta FIRE}$ brains.

(E) Reduced thalamic GFAP immunoreactivity in microglia-transplanted *Csf1r*$^{\Delta FIRE/\Delta FIRE}$ brains.

(F) Increased thalamic NeuN^{+} neurons per field of view (FOV) in microglia-injected *Csf1r*$^{\Delta FIRE/\Delta FIRE}$ brains.

(G) Reduced SERPINA3N levels in the fimbria of microglia-injected *Csf1r*$^{\Delta FIRE/\Delta FIRE}$ brains.

(H) Numbers of OLIG2^{+} oligodendrocytes do not differ per FOV in microglia-injected *Csf1r*$^{\Delta FIRE/\Delta FIRE}$ brains.

(I) Numbers of SMI312^{+} axonal spheroids per FOV are reduced in microglia-injected *Csf1r*$^{\Delta FIRE/\Delta FIRE}$ brains. *n*= 6–8 mice per group (3–4 males and females per group); groups compared by unpaired t tests; ****$p < 0.0001$; ***$p < 0.001$; *$p < 0.05$). Mean ± SEM shown for plotted data. Scale bars: 50 μm for (A) and (E)–(H); 1 mm for (C); 100 μm for (I) (20 μm for images in Ii and Iii).

The most striking abnormality observed with aging in *Csf1r*$^{\Delta FIRE/\Delta FIRE}$ brains was the dramatic acceleration and intensification of thalamic calcification, which was prevented by reconstituting *Csf1r*$^{\Delta FIRE/\Delta FIRE}$ mice with wild-type microglia. Around 30% of humans over 60 years of age have brain calcifications detectable by computerized tomography scanning, while calcification rates in those under 40 years of age are near zero.[58] Individuals with mutations causing either reduced microglial numbers or dysfunctional microglia (due to *CSF1R* and negative regulator of reactive oxygen species [*NRROS*] mutations, respectively) develop brain calcifications at young ages,[18,19,59] illustrating the relevance of our findings to microglial functions in humans. Additionally, recent findings demonstrate that microglia control vascular calcification in mouse models of PFBC,[46] a neurodegenerative disease characterized by small vessel calcification. These data suggest that microglia may hold promise as therapeutic targets in a wider range of neurodegenerative diseases.

The mechanisms underlying calcium phosphate deposition in the microglia-deficient thalamus and in the thalamus in normal aging require further investigation but could be due to several factors.[47] The thalamus may be a region of high calcium phosphate deposition due to normal cellular processes,[60,61] and the clearance of these deposits may be hindered in the absence of microglia. Alternatively, calcification formation can be initiated when non-osteogenic cells aberrantly adopt osteogenic traits.[62] We did not find evidence supporting this mechanism in our scRNA-seq dataset of the microglia-deficient thalamus. The expression of genes encoding calcification-associated proteins, such as osteopontin (*Spp1*) and osteocalcin (*Bglap*), was unaltered in the *Csf1r*$^{\Delta FIRE/\Delta FIRE}$ thalamus despite their considerable accumulation around calcifications. These findings raise questions regarding the source(s) of osteopontin, osteocalcin, and other bone-matrix proteins, as well as their precise roles in brain calcification formation in the absence/presence of microglia.

A limitation of this study is that relatively few neurons were captured in our scRNA-seq datasets. Evidence from recent reports indicates that neurons are altered in *Csf1r*$^{\Delta FIRE/\Delta FIRE}$ brains. For example, a prior study presented single-nuclei RNA

sequencing data from 5- to 6-month-old *Csf1r*$^{\Delta FIRE/\Delta FIRE}$ brains, revealing transcriptional changes in various neuronal subtypes.[55] Moreover, we recently reported deficits in excitatory neurotransmission in *Csf1r*$^{\Delta FIRE/\Delta FIRE}$ hippocampi, whereas we found no differences in synapse numbers, spine density, or neuronal morphology.[15] For the non-neuronal cell types we examined, further studies are necessary to establish links between the described RNA changes and alterations in their cellular functions. A further consideration is that we examined *Csf1r*$^{\Delta FIRE/\Delta FIRE}$ mice on a mixed C57BL/6JCrl and CBA/Ca genetic background, and it is possible that phenotype severity and age of onset due to microglial deficiencies may vary depending on the background of the mice.[63] Despite these points, we believe our profiling of various brain cell types and regions across the lifespan in the microglia-deficient brain will be a valuable resource for the field.

Taken together, our observations reveal a previously unappreciated requirement for microglia in safeguarding the brain parenchyma with aging. These findings also lend conceptual support to strategies aimed at replacing dysfunctional endogenous microglia, a concept further explored in the accompanying study by Chadarevian and colleagues.

STAR★METHODS

Detailed methods are provided in the online version of this paper and include the following:

- KEY RESOURCES TABLE
- RESOURCE AVAILABILITY
  - Lead contact
  - Materials availability
  - Data and code availability
- EXPERIMENTAL MODEL AND STUDY PARTICIPANT DETAILS
  - Animals (mice)
- METHOD DETAILS
  - Single-cell isolations and library preparation
  - Flow cytometry
  - Behavioral tests
  - *Ex vivo* MRI scanning
  - *In vivo* MRI scanning
  - Immunolabeling
  - Histological staining
  - Microglial transplantations
  - Hematology
- QUANTIFICATION AND STATISTICAL ANALYSIS
  - Single-cell RNA sequencing analysis
  - MRI analysis
  - Microscopy and image analysis
  - Statistical analyses
- ADDITIONAL RESOURCES
  - Interactive database

SUPPLEMENTAL INFORMATION

Supplemental information can be found online at https://doi.org/10.1016/j.neuron.2024.05.018.

ACKNOWLEDGMENTS

We thank Methodios Ximerakis for his advice regarding the brain dissociation protocol and Prakash Ramachandran for early discussions about scRNA-seq experiments. We thank Fiona Rossi of the Institute for Regeneration and Repair (IRR) Flow Cytometry Core Facility. MRI work was carried out on a 9.4T MRI scanner within the Edinburgh Preclinical Imaging Facility, University of Edinburgh. We thank Melanie McMillan and SURF @Edinburgh University for assistance with histology. We also thank Veronique Miron, Paola Cazzini, Philip Hasel, and William Mungall for discussions and assistance relating to this work. Funding: this work is supported by the UK Dementia Research Institute (DRI) through UK DRI Ltd., principally funded by the UK Medical Research Council (MRC), and additional funding partners ASUK and ARUK. J.P. is supported by a UK DRI Programme Award (award number UK DRI-4013) and by DFG CRC/TRR167 and BMBF/DLR FZ:01EE2303B. The work of A.M. is supported by the UK Dementia Research Institute, award number UK DRI-4011, and A.M. also holds a UKRI MRC fellowship (Career Development Award MR/V032488/1). B.W.M. is supported by the UK DRI (UK DRI-4005) and the Leducq Foundation Transatlantic Network of Excellence (19CVD01). A.W. is supported by the UK DRI, MRC, and MS Society UK. N.M. is a recipient of the grant/award numbers: BBS/E/RL/230001C and BB/S005471/1 from the Biotechnology and Biological Sciences Research Council. Part of the work was funded by a Seedcorn Award to from the RS Macdonald Charitable Trust to Edinburgh Neuroscience, University of Edinburgh. A.K. is funded by the Swiss National Science Foundation (310030_188952), Dementia Research Switzerland – Synapsis Foundation, and the Choupette Foundation (2019-PI02).

AUTHOR CONTRIBUTIONS

Conceptualization, D.A.D.M. and J.P.; methodology, D.A.D.M., N.B.-C., A. Chagnot, A. Corsinotti, A.W., R.J.L., and M.A.J.; software, N.B.-C. and A. Chagnot; validation, D.A.D.M., N.B.-C., and A. Corsinotti; formal analysis, D.A.D.M., N.B.-C., C.M., A. Chagnot, S.K.S., and J.P.C.; investigation, D.A.D.M., C.M., S.K.S., J.P.C., S.S., K.M., U.M., M.M., and B.B.; resources, J.P., C.P., M.B.-J., and A.M.; data curation, D.A.D.M., N.B.-C., R.J.L., and M.A.J.; writing – original draft, D.A.D.M.; writing – review & editing, D.A.D.M., N.B.-C., J.P.C., N.M., A.K., M.B.-J., and J.P.; visualization, D.A.D.M.; supervision, N.M., A.K., B.W.M., M.B.-J., A.M., A.W., and J.P.; funding acquisition, J.P.

DECLARATION OF INTERESTS

The authors declare no competing interests.

Received: November 16, 2023
Revised: April 17, 2024
Accepted: May 16, 2024
Published: June 18, 2024

REFERENCES

1. Chadarevian, J.P., Hasselmann, J., Lahian, A., Capocchi, J., Escobar, A., Lim, T.E., Le, L., Tu, C., Nguyen, J., Shabestari, S.K., et al. (2024). Therapeutic potential of human microglial transplantation in a chimeric model of CSF1R-related leukoencephalopathy. Neuron *112*. https://doi.org/10.1016/j.neuron.2024.05.023.
2. Borst, K., Dumas, A.A., and Prinz, M. (2021). Microglia: immune and non-immune functions. Immunity *54*, 2194–2208. https://doi.org/10.1016/j.immuni.2021.09.014.
3. Baxter, P.S., Dando, O., Emelianova, K., He, X., McKay, S., Hardingham, G.E., and Qiu, J. (2021). Microglial identity and inflammatory responses are controlled by the combined effects of neurons and astrocytes. Cell Rep. *34*, 108882. https://doi.org/10.1016/j.celrep.2021.108882.
4. Hammond, T.R., Dufort, C., Dissing-Olesen, L., Giera, S., Young, A., Wysoker, A., Walker, A.J., Gergits, F., Segel, M., Nemesh, J., et al. (2019). Single-cell RNA sequencing of microglia throughout the mouse lifespan and in the injured brain reveals complex cell-state changes. Immunity *50*, 253–271.e6. https://doi.org/10.1016/j.immuni.2018.11.004.
5. Pasciuto, E., Burton, O.T., Roca, C.P., Lagou, V., Rajan, W.D., Theys, T., Mancuso, R., Tito, R.Y., Kouser, L., Callaerts-Vegh, Z., et al. (2020).

Microglia require CD4 T cells to complete the fetal-to-adult transition. Cell *182*, 625–640.e24. https://doi.org/10.1016/j.cell.2020.06.026.

6. Hagemeyer, N., Hanft, K.-M., Akriditou, M.-A., Unger, N., Park, E.S., Stanley, E.R., Staszewski, O., Dimou, L., and Prinz, M. (2017). Microglia contribute to normal myelinogenesis and to oligodendrocyte progenitor maintenance during adulthood. Acta Neuropathol. *134*, 441–458. https://doi.org/10.1007/s00401-017-1747-1.
7. Nicholas, R.S., Wing, M.G., and Compston, A. (2001). Nonactivated microglia promote oligodendrocyte precursor survival and maturation through the transcription factor NF-kappa B. Eur. J. Neurosci. *13*, 959–967. https://doi.org/10.1046/j.0953-816x.2001.01470.x.
8. Pang, Y., Fan, L.-W., Tien, L.-T., Dai, X., Zheng, B., Cai, Z., Lin, R.C.S., and Bhatt, A. (2013). Differential roles of astrocyte and microglia in supporting oligodendrocyte development and myelination in vitro. Brain Behav. *3*, 503–514. https://doi.org/10.1002/brb3.152.
9. Schmidt, S.I., Bogetofte, H., Ritter, L., Agergaard, J.B., Hammerich, D., Kabiljagic, A.A., Wlodarczyk, A., Lopez, S.G., Sørensen, M.D., Jørgensen, M.L., et al. (2021). Microglia-secreted factors enhance dopaminergic differentiation of tissue- and iPSC-derived human neural stem cells. Stem Cell Rep. *16*, 281–294. https://doi.org/10.1016/j.stemcr.2020.12.011.
10. Rojo, R., Pridans, C., Langlais, D., and Hume, D.A. (2017). Transcriptional mechanisms that control expression of the macrophage colony-stimulating factor receptor locus. Clin. Sci. (Lond) *131*, 2161–2182. https://doi.org/10.1042/CS20170238.
11. Sasmono, R.T., Oceandy, D., Pollard, J.W., Tong, W., Pavli, P., Wainwright, B.J., Ostrowski, M.C., Himes, S.R., and Hume, D.A. (2003). A macrophage colony-stimulating factor receptor-green fluorescent protein transgene is expressed throughout the mononuclear phagocyte system of the mouse. Blood *101*, 1155–1163. https://doi.org/10.1182/blood-2002-02-0569.
12. Munro, D.A.D., Bradford, B.M., Mariani, S.A., Hampton, D.W., Vink, C.S., Chandran, S., Hume, D.A., Pridans, C., and Priller, J. (2020). CNS macrophages differentially rely on an intronic Csf1r enhancer for their development. Development *147*, dev194449. https://doi.org/10.1242/dev.194449.
13. Rojo, R., Raper, A., Ozdemir, D.D., Lefevre, L., Grabert, K., Wollscheid-Lengeling, E., Bradford, B., Caruso, M., Gazova, I., Sánchez, A., et al. (2019). Deletion of a Csf1r enhancer selectively impacts CSF1R expression and development of tissue macrophage populations. Nat. Commun. *10*, 3215. https://doi.org/10.1038/s41467-019-11053-8.
14. McNamara, N.B., Munro, D.A.D., Bestard-Cuche, N., Uyeda, A., Bogie, J.F.J., Hoffmann, A., Holloway, R.K., Molina-Gonzalez, I., Askew, K.E., Mitchell, S., et al. (2023). Microglia regulate central nervous system myelin growth and integrity. Nature *613*, 120–129. https://doi.org/10.1038/s41586-022-05534-y.
15. Surala, M., Soso-Zdravkovic, L., Munro, D., Rifat, A., Ouk, K., Vida, I., Priller, J., and Madry, C. (2024). Lifelong absence of microglia alters hippocampal glutamatergic networks but not synapse and spine density. EMBO Rep. *25*, 2348–2374. https://doi.org/10.1038/s44319-024-00130-9.
16. Elmore, M.R.P., Najafi, A.R., Koike, M.A., Dagher, N.N., Spangenberg, E.E., Rice, R.A., Kitazawa, M., Matusow, B., Nguyen, H., West, B.L., et al. (2014). Colony-stimulating Factor 1 receptor signaling is necessary for microglia viability, unmasking a microglia progenitor cell in the adult brain. Neuron *82*, 380–397. https://doi.org/10.1016/j.neuron.2014.02.040.
17. Erblich, B., Zhu, L., Etgen, A.M., Dobrenis, K., and Pollard, J.W. (2011). Absence of colony stimulation Factor-1 receptor results in loss of microglia, disrupted brain development and olfactory deficits. PLoS One *6*, e26317. https://doi.org/10.1371/journal.pone.0026317.
18. Guo, L., Bertola, D.R., Takanohashi, A., Saito, A., Segawa, Y., Yokota, T., Ishibashi, S., Nishida, Y., Yamamoto, G.L., Franco, J.F.D.S., et al. (2019). Bi-allelic CSF1R mutations cause skeletal dysplasia of Dysosteosclerosis-Pyle disease spectrum and degenerative encephalopathy with brain malformation. Am. J. Hum. Genet. *104*, 925–935. https://doi.org/10.1016/j.ajhg.2019.03.004.
19. Oosterhof, N., Chang, I.J., Karimiani, E.G., Kuil, L.E., Jensen, D.M., Daza, R., Young, E., Astle, L., van der Linde, H.C., Shivaram, G.M., et al. (2019). Homozygous mutations in CSF1R cause a pediatric-onset leukoencephalopathy and can result in congenital absence of microglia. Am. J. Hum. Genet. *104*, 936–947. https://doi.org/10.1016/j.ajhg.2019.03.010.
20. Marques, S., Zeisel, A., Codeluppi, S., van Bruggen, D., Mendanha Falcão, A., Xiao, L., Li, H., Häring, M., Hochgerner, H., Romanov, R.A., et al. (2016). Oligodendrocyte heterogeneity in the mouse juvenile and adult central nervous system. Science *352*, 1326–1329. https://doi.org/10.1126/science.aaf6463.
21. Dann, E., Henderson, N.C., Teichmann, S.A., Morgan, M.D., and Marioni, J.C. (2022). Differential abundance testing on single-cell data using k-nearest neighbor graphs. Nat. Biotechnol. *40*, 245–253. https://doi.org/10.1038/s41587-021-01033-z.
22. Nemes-Baran, A.D., White, D.R., and DeSilva, T.M. (2020). Fractalkine-dependent microglial pruning of viable oligodendrocyte progenitor cells regulates myelination. Cell Rep. *32*, 108047. https://doi.org/10.1016/j.celrep.2020.108047.
23. Santos, E.N., and Fields, R.D. (2021). Regulation of myelination by microglia. Sci. Adv. *7*, eabk1131. https://doi.org/10.1126/sciadv.abk1131.
24. Wlodarczyk, A., Holtman, I.R., Krueger, M., Yogev, N., Bruttger, J., Khorooshi, R., Benmamar-Badel, A., de Boer-Bergsma, J.J., Martin, N.A., Karram, K., et al. (2017). A novel microglial subset plays a key role in myelinogenesis in developing brain. EMBO J. *36*, 3292–3308. https://doi.org/10.15252/embj.201696056.
25. Chitu, V., Gokhan, S., Gulinello, M., Branch, C.A., Patil, M., Basu, R., Stoddart, C., Mehler, M.F., and Stanley, E.R. (2015). Phenotypic characterization of a Csf1r haploinsufficient mouse model of adult-onset leukodystrophy with axonal spheroids and pigmented glia (ALSP). Neurobiol. Dis. *74*, 219–228. https://doi.org/10.1016/j.nbd.2014.12.001.
26. Konno, T., Tada, M., Tada, M., Koyama, A., Nozaki, H., Harigaya, Y., Nishimiya, J., Matsunaga, A., Yoshikura, N., Ishihara, K., et al. (2014). Haploinsufficiency of CSF-1R and clinicopathologic characterization in patients with HDLS. Neurology *82*, 139–148. https://doi.org/10.1212/WNL.0000000000000046.
27. Berdowski, W.M., van der Linde, H.C., Breur, M., Oosterhof, N., Beerepoot, S., Sanderson, L., Wijnands, L.I., de Jong, P., Tsai-Meu-Chong, E., de Valk, W., et al. (2022). Dominant-acting CSF1R variants cause microglial depletion and altered astrocytic phenotype in zebrafish and adult-onset leukodystrophy. Acta Neuropathol. *144*, 211–239. https://doi.org/10.1007/s00401-022-02440-5.
28. Stables, J., Green, E.K., Sehgal, A., Patkar, O.L., Keshvari, S., Taylor, I., Ashcroft, M.E., Grabert, K., Wollscheid-Lengeling, E., Szymkowiak, S., et al. (2022). A kinase-dead Csf1r mutation associated with adult-onset leukoencephalopathy has a dominant inhibitory impact on CSF1R signalling. Development *149*, dev200237. https://doi.org/10.1242/dev.200237.
29. Falcão, A.M., van Bruggen, D., Marques, S., Meijer, M., Jäkel, S., Agirre, E., Samudyata, F., Floriddia, E.M., Vanichkina, D.P., Ffrench-Constant, C., et al. (2018). Disease-specific oligodendrocyte lineage cells arise in multiple sclerosis. Nat. Med. *24*, 1837–1844. https://doi.org/10.1038/s41591-018-0236-y.
30. Kenigsbuch, M., Bost, P., Halevi, S., Chang, Y., Chen, S., Ma, Q., Hajbi, R., Schwikowski, B., Bodenmiller, B., Fu, H., et al. (2022). A shared disease-associated oligodendrocyte signature among multiple CNS pathologies. Nat. Neurosci. *25*, 876–886. https://doi.org/10.1038/s41593-022-01104-7.
31. Hulsen, T. (2022). DeepVenn – a web application for the creation of area-proportional Venn diagrams using the deep learning framework Tensorflow. Preprint at arXiv. https://doi.org/10.48550/arXiv.2210.04597.
32. Liddelow, S.A., Guttenplan, K.A., Clarke, L.E., Bennett, F.C., Bohlen, C.J., Schirmer, L., Bennett, M.L., Münch, A.E., Chung, W.-S., Peterson, T.C.,

et al. (2017). Neurotoxic reactive astrocytes are induced by activated microglia. Nature *541*, 481–487. https://doi.org/10.1038/nature21029.

33. Brocker, C., Lassen, N., Estey, T., Pappa, A., Cantore, M., Orlova, V.V., Chavakis, T., Kavanagh, K.L., Oppermann, U., and Vasiliou, V. (2010). Aldehyde dehydrogenase 7A1 (ALDH7A1) is a novel enzyme involved in cellular defense against hyperosmotic stress. J. Biol. Chem. *285*, 18452–18463. https://doi.org/10.1074/jbc.M109.077925.
34. Noubade, R., Wong, K., Ota, N., Rutz, S., Eidenschenk, C., Valdez, P.A., Ding, J., Peng, I., Sebrell, A., Caplazi, P., et al. (2014). NRROS negatively regulates reactive oxygen species during host defence and autoimmunity. Nature *509*, 235–239. https://doi.org/10.1038/nature13152.
35. Hou, J., Zhou, Y., Cai, Z., Terekhova, M., Swain, A., Andhey, P.S., Guimaraes, R.M., Ulezko Antonova, A., Qiu, T., Sviben, S., et al. (2023). Transcriptomic atlas and interaction networks of brain cells in mouse CNS demyelination and remyelination. Cell Rep. *42*, 112293. https://doi.org/10.1016/j.celrep.2023.112293.
36. Hasel, P., Rose, I.V.L., Sadick, J.S., Kim, R.D., and Liddelow, S.A. (2021). Neuroinflammatory astrocyte subtypes in the mouse brain. Nat. Neurosci. *24*, 1475–1487. https://doi.org/10.1038/s41593-021-00905-6.
37. Patkar, O.L., Caruso, M., Teakle, N., Keshvari, S., Bush, S.J., Pridans, C., Belmer, A., Summers, K.M., Irvine, K.M., and Hume, D.A. (2021). Analysis of homozygous and heterozygous Csf1r knockout in the rat as a model for understanding microglial function in brain development and the impacts of human CSF1R mutations. Neurobiol. Dis. *151*, 105268. https://doi.org/10.1016/j.nbd.2021.105268.
38. Thomas, B., Somasundaram, S., Thamburaj, K., Kesavadas, C., Gupta, A.K., Bodhey, N.K., and Kapilamoorthy, T.R. (2008). Clinical applications of susceptibility weighted MR imaging of the brain - a pictorial review. Neuroradiology *50*, 105–116. https://doi.org/10.1007/s00234-007-0316-z.
39. Fraser, H. (1968). Bilateral thalamic calcification in ageing mice. J. Pathol. Bacteriol. *96*, 220–222. https://doi.org/10.1002/path.1700960124.
40. Morgan, K.T., Johnson, B.P., Frith, C.H., and Townsend, J. (1982). An ultrastructural study of spontaneous mineralization in the brains of aging mice. Acta Neuropathol. *58*, 120–124. https://doi.org/10.1007/BF00691652.
41. Yanai, T., Yamoto, T., Manabe, J., Takaoka, M., and Matsunuma, N. (1987). X-ray microanalysis of mineralization in the thalamus of aged mice. Nihon Juigaku. Nihon Juigaku Zasshi *49*, 920–922. https://doi.org/10.1292/jvms1939.49.920.
42. Yang, A.C., Stevens, M.Y., Chen, M.B., Lee, D.P., Stähli, D., Gate, D., Contrepois, K., Chen, W., Iram, T., Zhang, L., et al. (2020). Physiological blood-brain transport is impaired with age by a shift in transcytosis. Nature *583*, 425–430. https://doi.org/10.1038/s41586-020-2453-z.
43. Dietrich, P., Johnson, I.M., Alli, S., and Dragatsis, I. (2017). Elimination of huntingtin in the adult mouse leads to progressive behavioral deficits, bilateral thalamic calcification, and altered brain iron homeostasis. PLoS Genet. *13*, e1006846. https://doi.org/10.1371/journal.pgen.1006846.
44. Kalueff, A., Loseva, E., Haapasalo, H., Rantala, I., Keranen, J., Lou, Y.-R., Minasyan, A., Keisala, T., Miettinen, S., Kuuslahti, M., et al. (2006). Thalamic calcification in vitamin D receptor knockout mice. NeuroReport *17*, 717–721. https://doi.org/10.1097/01.wnr.0000215770.79281.e4.
45. Ni, R., Zarb, Y., Kuhn, G.A., Müller, R., Yundung, Y., Nitsch, R.M., Kulic, L., Keller, A., and Klohs, J. (2020). SWI and phase imaging reveal intracranial calcifications in the P301L mouse model of human Tauopathy. Magma *33*, 769–781. https://doi.org/10.1007/s10334-020-00855-3.
46. Zarb, Y., Sridhar, S., Nassiri, S., Utz, S.G., Schaffenrath, J., Maheshwari, U., Rushing, E.J., Nilsson, K.P.R., Delorenzi, M., Colonna, M., et al. (2021). Microglia control small vessel calcification via TREM2. Sci. Adv. *7*, eabc4898. https://doi.org/10.1126/sciadv.abc4898.
47. Maheshwari, U., Huang, S.-F., Sridhar, S., and Keller, A. (2022). The interplay between brain vascular calcification and microglia. Front. Aging Neurosci. *14*, 848495. https://doi.org/10.3389/fnagi.2022.848495.
48. Herrmann, J.E., Imura, T., Song, B., Qi, J., Ao, Y., Nguyen, T.K., Korsak, R.A., Takeda, K., Akira, S., and Sofroniew, M.V. (2008). STAT3 is a critical regulator of astrogliosis and scar formation after spinal cord injury. J. Neurosci. *28*, 7231–7243. https://doi.org/10.1523/JNEUROSCI.1709-08.2008.
49. Beck, H., Semisch, M., Culmsee, C., Plesnila, N., and Hatzopoulos, A.K. (2008). Egr-1 regulates expression of the glial scar component phosphacan in astrocytes after experimental stroke. Am. J. Pathol. *173*, 77–92. https://doi.org/10.2353/ajpath.2008.070648.
50. Muhl, L., Genové, G., Leptidis, S., Liu, J., He, L., Mocci, G., Sun, Y., Gustafsson, S., Buyandelger, B., Chivukula, I.V., et al. (2020). Single-cell analysis uncovers fibroblast heterogeneity and criteria for fibroblast and mural cell identification and discrimination. Nat. Commun. *11*, 3953. https://doi.org/10.1038/s41467-020-17740-1.
51. Taylor, E.N., Huang, N., Wisco, J., Wang, Y., Morgan, K.G., and Hamilton, J.A. (2020). The brains of aged mice are characterized by altered tissue diffusion properties and cerebral microbleeds. J. Transl. Med. *18*, 277. https://doi.org/10.1186/s12967-020-02441-6.
52. Wang, Y., Taylor, E., Zikopoulos, B., Seta, F., Huang, N., Hamilton, J.A., Kantak, K.M., and Morgan, K.G. (2021). Aging-induced microbleeds of the mouse thalamus compared to sensorimotor and memory defects. Neurobiol. Aging *100*, 39–47. https://doi.org/10.1016/j.neurobiolaging.2020.11.017.
53. Roelofs, A.J., Coxon, F.P., Ebetino, F.H., Lundy, M.W., Henneman, Z.J., Nancollas, G.H., Sun, S., Blazewska, K.M., Bala, J.L.F., Kashemirov, B.A., et al. (2010). Fluorescent risedronate analogues reveal bisphosphonate uptake by bone marrow monocytes and localization around osteocytes in vivo. J. Bone Miner. Res. *25*, 606–616. https://doi.org/10.1359/jbmr.091009.
54. Maheshwari, U., Mateos, J.M., Weber-Stadlbauer, U., Ni, R., Tamatey, V., Sridhar, S., Restrepo, A., de Jong, P.A., Huang, S.-F., Schaffenrath, J., et al. (2023). Inorganic phosphate exporter heterozygosity in mice leads to brain vascular calcification, microangiopathy, and microgliosis. Brain Pathol. *33*, e13189. https://doi.org/10.1111/bpa.13189.
55. Kiani Shabestari, S., Morabito, S., Danhash, E.P., McQuade, A., Sanchez, J.R., Miyoshi, E., Chadarevian, J.P., Claes, C., Coburn, M.A., Hasselmann, J., et al. (2022). Absence of microglia promotes diverse pathologies and early lethality in Alzheimer's disease mice. Cell Rep. *39*, 110961. https://doi.org/10.1016/j.celrep.2022.110961.
56. Papapetropoulos, S., Pontius, A., Finger, E., Karrenbauer, V., Lynch, D.S., Brennan, M., Zappia, S., Koehler, W., Schoels, L., Hayer, S.N., et al. (2021). Adult-onset leukoencephalopathy with axonal spheroids and pigmented glia: review of clinical manifestations as foundations for therapeutic development. Front. Neurol. *12*, 788168. https://doi.org/10.3389/fneur.2021.788168.
57. Masliah, E., Mallory, M., Hansen, L., Alford, M., DeTeresa, R., and Terry, R. (1993). An antibody against phosphorylated neurofilaments identifies a subset of damaged association axons in Alzheimer's disease. Am. J. Pathol. *142*, 871–882.
58. Nicolas, G., Pottier, C., Charbonnier, C., Guyant-Maréchal, L., Le Ber, I., Pariente, J., Labauge, P., Ayrignac, X., Defebvre, L., Maltête, D., et al. (2013). Phenotypic spectrum of probable and genetically-confirmed idiopathic basal ganglia calcification. Brain *136*, 3395–3407. https://doi.org/10.1093/brain/awt255.
59. Macintosh, J., Derksen, A., Poulin, C., Braverman, N., Vanderver, A., Thiffault, I., Albrecht, S., and Bernard, G. (2022). Novel biallelic variants in NRROS associated with a lethal Microgliopathy, brain calcifications, and neurodegeneration. Neurogenetics *23*, 151–156. https://doi.org/10.1007/s10048-022-00683-8.
60. Aggarwal, M., Li, X., Gröhn, O., and Sierra, A. (2018). Nuclei-specific deposits of iron and calcium in the rat thalamus after status epilepticus revealed with quantitative susceptibility mapping (QSM). J. Magn. Reson. Imaging *47*, 554–564. https://doi.org/10.1002/jmri.25777.

61. Kim, K.M. (1995). Apoptosis and calcification. Scan. Microsc. *9*, 1137–1175.

62. Pillai, I.C.L., Li, S., Romay, M., Lam, L., Lu, Y., Huang, J., Dillard, N., Zemanova, M., Rubbi, L., Wang, Y., et al. (2017). Cardiac fibroblasts adopt osteogenic fates and can be targeted to attenuate pathological heart calcification. Cell Stem Cell *20*, 218–232.e5. https://doi.org/10.1016/j.stem.2016.10.005.

63. Hume, D.A., Caruso, M., Ferrari-Cestari, M., Summers, K.M., Pridans, C., and Irvine, K.M. (2020). Phenotypic impacts of CSF1R deficiencies in humans and model organisms. J. Leukoc. Biol. *107*, 205–219. https://doi.org/10.1002/JLB.MR0519-143R.

64. Bankhead, P., Loughrey, M.B., Fernández, J.A., Dombrowski, Y., McArt, D.G., Dunne, P.D., McQuaid, S., Gray, R.T., Murray, L.J., Coleman, H.G., et al. (2017). QuPath: open source software for digital pathology image analysis. Sci. Rep. *7*, 16878. https://doi.org/10.1038/s41598-017-17204-5.

65. McCarthy, D.J., Campbell, K.R., Lun, A.T.L., and Wills, Q.F. (2017). Scater: pre-processing, quality control, normalization and visualization of single-cell RNA-seq data in R. Bioinform. Oxf. Engl. *33*, 1179–1186. https://doi.org/10.1093/bioinformatics/btw777.

66. Lun, A.T.L., Bach, K., and Marioni, J.C. (2016). Pooling across cells to normalize single-cell RNA sequencing data with many zero counts. Genome Biol. *17*, 75. https://doi.org/10.1186/s13059-016-0947-7.

67. Hao, Y., Hao, S., Andersen-Nissen, E., Mauck, W.M., Zheng, S., Butler, A., Lee, M.J., Wilk, A.J., Darby, C., Zager, M., et al. (2021). Integrated analysis of multimodal single-cell data. Cell *184*, 3573–3587.e29. https://doi.org/10.1016/j.cell.2021.04.048.

68. Germain, P.-L., Lun, A., Garcia Meixide, C., Macnair, W., and Robinson, M.D. (2021). Doublet identification in single-cell sequencing data using scDblFinder. F1000Res *10*, 979. https://doi.org/10.12688/f1000research.73600.2.

69. Zappia, L., and Oshlack, A. (2018). Clustering trees: A visualization for evaluating clusterings at multiple resolutions. GigaScience *7*, giy083. https://doi.org/10.1093/gigascience/giy083.

70. Lun, A.T.L., Riesenfeld, S., Andrews, T., Dao, T.P., Gomes, T.; participants in the 1st Human Cell Atlas Jamboree, and Marioni, J.C. (2019). EmptyDrops: distinguishing cells from empty droplets in droplet-based single-cell RNA sequencing data. Genome Biol. *20*, 63. https://doi.org/10.1186/s13059-019-1662-y.

71. Street, K., Risso, D., Fletcher, R.B., Das, D., Ngai, J., Yosef, N., Purdom, E., and Dudoit, S. (2018). Slingshot: cell lineage and pseudotime inference for single-cell transcriptomics. BMC Genomics *19*, 477. https://doi.org/10.1186/s12864-018-4772-0.

72. Ouyang, J.F., Kamaraj, U.S., Cao, E.Y., and Rackham, O.J.L. (2021). ShinyCell: simple and sharable visualization of single-cell gene expression data. Bioinform. Oxf. Engl. *37*, 3374–3376. https://doi.org/10.1093/bioinformatics/btab209.

73. Haghverdi, L., Lun, A.T.L., Morgan, M.D., and Marioni, J.C. (2018). Batch effects in single-cell RNA-sequencing data are corrected by matching mutual nearest neighbors. Nat. Biotechnol. *36*, 421–427. https://doi.org/10.1038/nbt.4091.

74. Korsunsky, I., Millard, N., Fan, J., Slowikowski, K., Zhang, F., Wei, K., Baglaenko, Y., Brenner, M., Loh, P.R., and Raychaudhuri, S. (2019). Fast, sensitive and accurate integration of single-cell data with harmony. Nat. Methods *16*, 1289–1296. https://doi.org/10.1038/s41592-019-0619-0.

75. Hasselmann, J., Coburn, M.A., England, W., Figueroa Velez, D.X., Kiani Shabestari, S., Tu, C.H., McQuade, A., Kolahdouzan, M., Echeverria, K., Claes, C., et al. (2019). Development of a chimeric model to study and manipulate human microglia in vivo. Neuron *103*, 1016–1033.e10. https://doi.org/10.1016/j.neuron.2019.07.002.

76. Van Der Maaten, L., and Hinton, G. (2008). Visualizing data using T-SNE. J. Mach. Learn. Res. *9*, 2579–2605.

77. McInnes, L., Healy, J., Saul, N., and Großberger, L. (2018). UMAP: uniform manifold approximation and projection. JOSS *3*, 861. https://doi.org/10.21105/joss.00861.

78. Ximerakis, M., Lipnick, S.L., Innes, B.T., Simmons, S.K., Adiconis, X., Dionne, D., Mayweather, B.A., Nguyen, L., Niziolek, Z., Ozek, C., et al. (2019). Single-cell transcriptomic profiling of the aging mouse brain. Nat. Neurosci. *22*, 1696–1708. https://doi.org/10.1038/s41593-019-0491-3.

79. Robinson, M.D., McCarthy, D.J., and Smyth, G.K. (2010). edgeR: A bioconductor package for differential expression analysis of digital gene expression data. Bioinformatics *26*, 139–140. https://doi.org/10.1093/bioinformatics/btp616.

80. Soneson, C., and Robinson, M.D. (2018). Bias, robustness and scalability in single-cell differential expression analysis. Nat. Methods *15*, 255–261. https://doi.org/10.1038/nmeth.4612.

81. Dorr, A.E., Lerch, J.P., Spring, S., Kabani, N., and Henkelman, R.M. (2008). High resolution three-dimensional brain atlas using an average magnetic resonance image of 40 adult C57BL/6J mice. NeuroImage *42*, 60–69. https://doi.org/10.1016/j.neuroimage.2008.03.037.

82. Belle, V., Kahler, E., Waller, C., Rommel, E., Voll, S., Hiller, K.H., Bauer, W.R., and Haase, A. (1998). In vivo quantitative mapping of cardiac perfusion in rats using a noninvasive MR spin-labeling method. J. Magn. Reson. Imaging *8*, 1240–1245. https://doi.org/10.1002/jmri.1880080610.

Please cite this article in press as: Munro et al., Microglia protect against age-associated brain pathologies, Neuron (2024), https://doi.org/10.1016/j.neuron.2024.05.018

STAR★METHODS

KEY RESOURCES TABLE

REAGENT or RESOURCE	SOURCE	IDENTIFIER
Antibodies		
Rat PE anti-CD11b	BioLegend	Cat# 101207, RRID:AB_312790
Rat PE/Cyanine7 anti-CD45	BioLegend	Cat# 103114, RRID:AB_312979
Rat APC anti-CD115	BioLegend	Cat# 135510, RRID:AB_2085221
Rat anti-GFAP	Thermo Fisher	Cat# 13-0300, RRID:AB_2532994
Goat anti-SERPINA3N	R and D systems	Cat# AF4709, RRID:AB_2270116
Rabbit anti-NeuN	Abcam	Cat# ab177487, RRID:AB_2532109
Goat anti-osteopontin	R and D systems	Cat# AF808, RRID:AB_2194992
Rabbit anti-IBA1	FUJIFILM Wako Pure Chemical Corporation	Cat# 019-19741, RRID:AB_839504
Rabbit anti-OLIG2	Millipore	Cat# AB9610, RRID:AB_570666
Rabbit anti-SOX10	Abcam	Cat# ab155279, RRID:AB_2650603
Rabbit anti-Fibrinogen	Agilent	Cat# A008002, RRID:AB_578481
Rat anti-CD31	BD Biosciences	Cat# 553370, RRID:AB_394816
Goat anti-CD13	R and D systems	Cat# AF2335, RRID:AB_2227288
Mouse anti-β-dystroglycan	Santa Cruz Biotechnology	Cat# sc-33702, RRID:AB_627292
Rabbit anti-ERG	Abcam	Cat# ab92513, RRID:AB_2630401
Goat anti-IBA1	Abcam	Cat# ab5076, RRID:AB_2224402
Rabbit anti-aquaporin 4	Novus	Cat# NBP1-87679, RRID:AB_11006038
Rabbit anti-APP	Thermo Fisher Scientific	Cat# PA5-19923, RRID:AB_11152072
Goat anti-osteocalcin	Thermo Scientific Alfa Aesar	Cat# J65216
Goat anti-osteopontin	R and D systems	Cat# AF808, RRID:AB_2194992
Rat anti-CD31	Dianova	Cat# DIA-310, RRID:AB_2631039
Goat anti-CD206	R and D systems	Cat# AF2535; RRID:AB_2063012
Rabbit anti-IBA1	Abcam	Cat# ab178846; RRID:AB_2636859
Mouse anti-Neurofilament (SMI312)	Biolegend	Cat# 837904; RRID:AB_2566782
Rabbit anti-NeuN	Abcam	Cat# abn78; RRID:AB_10807945
Chicken anti-GFAP	Abcam	Cat# ab4674; RRID:AB_304558
Goat anti-OLIG2	R and D systems	Cat# AF2418; RRID:AB_2157554
Biological samples		
C57BL/6 primary mouse microglia	ScienCell	Cat# M1900-57
Chemicals, peptides, and recombinant proteins		
Actinomycin D	Sigma	Cat# A1410
Trehalose dihydrate	Sigma	Cat# T0167
MultiHance® (gadobenate dimeglumine)	Bracco	Cat# 0270-5164
AF647-RIS	Biovinc	Cat# BV500101
5-FAM-Zol	Biovinc	Cat# BV111001
Alizarin Red S	Millipore-Sigma	Cat# TMS-008
Perl's Prussian Blue	TCS Biosciences	Cat# HS652
Microglial media	ScienCell	Cat# 1901
DPX mounting media	CellPath	Cat# SEA-1304-00A
ProLong™ Gold Antifade Mountant	Invitrogen	Cat# P36930
Critical commercial assays		
Adult brain dissociation kit	Miltenyi Biotec	Cat# 130-107-677

(*Continued on next page*)

Continued

REAGENT or RESOURCE	SOURCE	IDENTIFIER
Chromium Single Cell 3′ Reagent Kit v.3.1	10x Genomics	Cat# PN-1000121
Chromium Next GEM Chip G kit	10x Genomics	Cat# PN-1000120
Deposited data		
Raw and analyzed data	This paper	GEO: GSE267545
Analyzed scRNA-seq data (from 6- to 7-week-old *Csf1r*$^{WT/WT}$ and *Csf1r*$^{\Delta FIRE/\Delta FIRE}$ samples)	McNamara et al.[14]	GEO: GSE215440
Experimental models: Organisms/strains		
Csf1r$^{\Delta FIRE/\Delta FIRE}$ mice	Rojo et al.[13]	N/A
Software and algorithms		
Imaris, version 9.9	Oxford Instruments	https://imaris.oxinst.com/
Fiji (Image J), version 2.0.0 – 2.3.0	NIH	https://imagej.nih.gov/ij/
QuPath, version 0.4.3	Bankhead et al.[64]	https://qupath.github.io/
Ingenuity Pathway Analysis	Qiagen	https://digitalinsights.qiagen.com/
Prism, version 10	GraphPad	https://www.graphpad.com/
FCS express 7	De Novo software	https://denovosoftware.com/
CatWalk XT gait analysis	Noldus	https://www.noldus.com/catwalk-xt
Any-Maze video tracking software (v.6.3)	Stoelting Europe	https://www.any-maze.com/
CellRanger (v5.0.0-v7.0.0)	10x Genomics	https://www.10xgenomics.com/support/software/cell-ranger/latest
MATLAB	The MathWorks, Inc	https://www.mathworks.com/products/matlab.html
Bruker's Paravision 360	Bruker	https://www.bruker.com/en.html
R v.4.1.1-v.4.2.1-v.4.3.1	CRAN	https://cran.r-project.org/
Scater	McCarthy et al.[65]	https://bioconductor.org/packages/release/bioc/html/scater.html
Scran	Lun et al.[66]	https://bioconductor.org/packages/release/bioc/html/scran.html
Seurat	Hao et al.[67]	https://satijalab.org/seurat/
scDblFinder	Germain et al.[68]	https://bioconductor.org/packages/release/bioc/html/scDblFinder.html
clustree	Zappia and Oshlack[69]	https://github.com/lazappi/clustree
Milo	Dann et al.[21]	https://github.com/MarioniLab/miloR
DropletUtils	Lun et al.[70]	https://bioconductor.org/packages/release/bioc/html/DropletUtils.html
VasOMatic v1.0	Audrey Chagnot	https://doi.org/10.5281/zenodo.11198372
Slingshot (v 2.0.0)	Street et al.[71]	https://bioconductor.org/packages/release/bioc/html/slingshot.html
ShinyCell	Ouyang et al.[72]	https://github.com/SGDDNB/ShinyCell
batchelor	Haghverdi et al.[73]	https://bioconductor.org/packages/release/bioc/html/batchelor.html
harmony	Korsunsky et al.[74]	https://portals.broadinstitute.org/harmony/
Fluoview FV31S-DT software	Olympus	https://www.olympus-lifescience.com/en/downloads/detail-iframe/?0[downloads][id]=847252002
Custom code	This paper	https://doi.org/10.5281/zenodo.11198851
Other		
Interactive databases for mining of sequencing data	This paper	https://annawilliams.shinyapps.io/shinyApp_jpriller/ https://annawilliams.shinyapps.io/shinyApp_jpriller/
Computer cluster - Eddie	Edinburgh Compute and Data Facility (ECDF)	http://www.ecdf.ed.ac.uk/

RESOURCE AVAILABILITY

Lead contact

Requests for further information, resources, and/or reagents should be directed to the lead contact, Josef Priller (josef.priller@ed.ac.uk).

Materials availability

This study did not generate new unique reagents.

Data and code availability

- Single-cell RNA-seq data have been deposited at GEO and are publicly available as of the date of publication. Accession numbers are listed in the key resources table. The cellranger matrices, cell information, and sample metadata are available at GEO: GSE267545 and at https://doi.org/10.5281/zenodo.11198851. We also provide an online resource to visualise the single-cell RNA-sequencing data generated for this manuscript (https://annawilliams.shinyapps.io/shinyApp_jpriller/). Microscopy and MRI data reported in this paper will be shared by the lead contact upon request.
- All original code has been deposited at Zenodo and is publicly available as of the date of publication. DOIs are listed in the key resources table.
- Any additional information required to reanalyse the data reported in this paper is available from the lead contact upon request.

EXPERIMENTAL MODEL AND STUDY PARTICIPANT DETAILS

Animals (mice)

Mice were bred and maintained under specific pathogen-free conditions in temperature- and humidity-controlled rooms in accordance with institutional guidelines. Mice were bred and maintained in 12 h light and dark cycles with chow and water provided ad libitum. *Csf1r*$^{\Delta FIRE}$ mice used in this study were on a mixed C57BL/6JCrl and CBA/Ca genetic background, as originally described in Rojo et al.[13] Group sizes, ages, and numbers of males/females used for each experiment are provided in respective figure legends. In cases where mice of both sexes were used in an experiment, we were underpowered to confidently report on any influence (or association) of sex on the findings. Mice were culled by qualified staff of a UK home office-licenced animal house and experiments were carried out under the authority of a UK Home Office Project License following guidelines set under the Animal (Scientific Procedures) Act 1986.

For the microglial transplantation experiments, all animal procedures were conducted in accordance with the guidelines set forth by the National Institutes of Health (NIH) and the University of California, Irvine Institutional Animal Care and Use Committee. Equivalent numbers of male and female mice were used, and all groups were age matched and group housed on a 12h/12h light/dark cycle with food and water ad libitum. *Csf1r*$^{\Delta FIRE}$ mice for this experiment were originally generated on a B6CBAF1/J background. Founders were then crossed with C57BL/6J mice for two generations and their offspring interbred.

METHOD DETAILS

Single-cell isolations and library preparation

Brain tissue harvests and dissociations were performed starting at approximately the same time of day for all mice (09:00–10:00 am). Processing of mice with different genotypes was mixed in a manner designed to reduce batch effects. Mice were culled via cervical dislocation and immediately processed without perfusion to reduce processing times. For 6-7-week-old "juvenile" samples, hippocampi from both hemispheres and the remainder of the left hemisphere were dissected (after removal of olfactory bulbs and cerebellum) and separately placed in 50 ml conical tubes containing 2 ml ice-cold HBSS (w/o $Ca2^{+}$ and $Mg2^{+}$, with 5% trehalose, 30 μM actinomycin D; A1410, Sigma) and finely minced using a disposable 22A scalpel to ensure rapid cooling. Hippocampi were processed separately to examine whether impacts of microglia deficiencies were particularly strong in this region compared to the rest of the brain. The same steps were carried out for all other single-cell RNA sequencing datasets: for the 11-12-months-old "adult" samples, the left hemisphere was processed (after removal of olfactory bulbs and cerebellum); for the 16-18-months-old "old" samples, the whole brain was processed (after removal of olfactory bulbs and cerebellum); for the 17-19-months-old "thalamus" samples, thalami were dissected from both hemispheres and processed. Although care was taken during hippocampal and thalamic dissections, it is possible that small numbers of cells from adjacent tissues may have unintentionally been retained.

Following tissue mincing, the dissociation protocol was performed as previously described[14] to generate brain single-cell suspensions. Brains were digested using the Adult Brain Dissociation Kit (130-107-677, Miltenyi Biotec) with the following modifications: (1) tissues were dissociated as described in the "manual dissociation" section of the Neural Tissue Dissociation Kit protocol (130-092-628, Miltenyi Biotec); (2) enzymatic digestions were performed at 35°C; (3) half the concentration of enzyme P was used; (4) actinomycin D was used to limit dissociation-induced transcriptional changes; (5) 5% trehalose was added in all buffers to increase cellular viability; (6) cell clusters were removed by filtration through pre-moistened 70 μm (352350, Falcon) and 40 μm (352340; Falcon) cell strainers; (7) erythrocyte and myelin debris removal steps were omitted; and (8) all centrifugations were performed at 200 g at 4°C.

Please cite this article in press as: Munro et al., Microglia protect against age-associated brain pathologies, Neuron (2024), https://doi.org/10.1016/j.neuron.2024.05.018

After generating a single cell suspension, cells were collected in PBS with 0.2% BSA before being sorted on a Sony SH800 cell sorter or a BD FACSAria II cell sorter. Gates were chosen based on forward and side scatter to include live cells (based on trial experiments; Figure S1A), while excluding doublets, erythrocytes, and debris using FSC and SSC parameters (Figure S1B). Non-viable cells were excluded based on DRAQ7 and/or DAPI staining. After confirming the post-sorting viability of cells, using trypan blue and a haemocytometer, single cells were processed through the Chromium Single Cell Platform using a Chromium Next GEM Single Cell 3′ GEM Library and Gel Bead kit (v.3.1 chemistry, PN-1000121, 10x genomics) and a Chromium Next GEM Chip G kit (PN-1000120) and processed following the manufacturer's instructions. Libraries were sequenced using a NovaSeq 6000 sequencing system (PE150 (HiSeq), Illumina).

Flow cytometry

To characterise CD115 expression levels, an enzyme-free dissociation protocol was used to isolate and characterise brain myeloid cells from 10–11-week-old female mice. Mice were transcardially perfused with ice-cold PBS. Brains were then dissected and minced with a 22A scalpel in HBSS (w/o Ca^{2+} and Mg^{2+}; 14175-053, Gibco) with 25 mM HEPES (10041703, Fisher Scientific). Samples were then homogenised with a Dounce homogeniser (D9938, Kimble) in HBSS (w/o $Ca2^{+}$ and $Mg2^{+}$) with 25 mM HEPES. Brain homogenates were separated using a 35% Percoll gradient, with centrifugation at 800 g for 20 min at 4 °C (with a slow acceleration/deceleration). Cell pellets were collected and washed in PBS (w/o $Ca2^{+}$ and $Mg2^{+}$; 14190-094, Gibco) with 0.1% low endotoxin BSA (A8806, Sigma Aldrich). Fc receptors were blocked (1:100; 101302, BioLegend) for 15 min at 4°C on a shaker. Cells were stained with primary antibodies directed against CD11b (PE; 1:200; 101207; BioLegend, clone M1/70), CD45 (PECy7; 1:200; 103114; BioLegend, clone 30-F11) and CD115 (APC; 1:200; 135510; BioLegend, clone AFS98) for 30 min at 4°C on a shaker. Samples were then washed and resuspended in PBS (w/o Ca^{2+} and Mg^{2+}) with 0.1% low endotoxin BSA. DAPI was used for viability gating. Single-fluorochrome stained beads, unstained samples, and fluorescence-minus-one samples were used as controls. Data were acquired using a BD LSRFortessa flow cytometer. FCS express 7 was used for data analysis. Data from the *Csf1r*$^{WT/WT}$ brain myeloid cells in this experiment were previously compared to *Csf1r*$^{\Delta FIRE/\Delta FIRE}$ brain myeloid cells.[14]

Behavioral tests

Juvenile behavioural studies were performed on mice of both sexes, with females and males being tested on different days and analysed separately. Mice were between 4-8 weeks of age when tested. Mice were housed under standard conditions with 12-hour light/dark cycles in temperature and humidity-controlled rooms. Experimenters were blinded to genotypes and remained blinded during data analysis. Handling was carried out 3-4 days prior to testing to minimise stress during testing. Open-field tests were carried out first, followed by the elevated plus maze. Equipment was cleaned with 70% ethanol between tests. No outliers were removed (based on lack of significance using Grubb's outlier testing). For open field testing, mice were placed in a 47 x 47 cm field to freely explore for 10 min. Total ambulatory distance travelled (in metres) and time spent in the edges (9 cm from the wall) and centre (29 × 29 cm) were quantified. For the elevated plus maze, the maze had four arms: two open, and two enclosed by walls. Mice were left to explore the maze for 5 min. Mice that fell from the maze during the test run were excluded from analyses. A camera was set up directly above the open field and elevated plus maze, and Any-Maze video tracking software (Stoelting Europe, v.6.3) was used to quantify exploration in the different regions of the field/maze.

For behavioural testing of aged mice, open field testing was performed first, followed by the CatWalk XT gait analysis. The open field test was performed as described above, with the exception that old males and females were not tested or analysed separately. The CatWalk XT gait analysis was performed on a glass plate walkway equipped with light-emitting diodes, which were used to identify paw contact points on the plate. A camera positioned underneath the glass plate captured images for analysis. Animals walked along the walkway 3 times on the day before evaluation to habituate them. On the testing day, recordings were repeated until three satisfactory walks were obtained. Trial statistics for each mouse were based on averaged values from 3 satisfactory runs.

Ex vivo MRI scanning

Mice were anaesthetised with isoflurane before being transcardially perfused with PBS (Ca^{2+}/Mg^{2+} free) with 0.05% heparin. Mice were then immediately perfusion fixed with 4% PFA in PBS (Ca^{2+}/Mg^{2+} free), which was pre-warmed to 37°C. Samples were prepared by dissecting surrounding hair, skin, and muscles from heads, while leaving the brain within the cranial vault. Samples were then immersion fixed in 4% PFA in PBS (Ca^{2+}/Mg^{2+} free) overnight, before being immersed in PBS (Ca^{2+}/Mg^{2+} free) with 0.01% sodium azide and placed on a rocker at 4°C for several days to leach out any remaining PFA (with the PBS solution being changed several times). Samples were then transferred to a 2.5 mM solution of the gadolinium-based contrast agent, gadobenate dimeglumine (MultiHance, Bracco Diagnostics Inc., Milan, Italy), with 0.01% sodium azide in PBS (Ca^{2+}/Mg^{2+} free) and placed on a rocker at 4°C for a further 24-48 hr prior to imaging.

MRI was performed using a 9.4T horizontal bore Biospec AVANCE neo preclinical imaging system equipped with a 116 mm bore gradient insert (Bruker BioSpin GmbH, Germany, maximum gradient strength 660 mT/m). For scanning, samples were immersed in Fomblin in 15 ml tubes and secured in place using plastic wedges. An 86 mm quadrature volume coil was used for transmission with signal reception by a four-channel phased-array mouse brain coil (Bruker BioSpin GmbH, Germany). Scout images were taken to confirm correct positioning, and the magnetic field was optimised using automated 3D field mapping routine.

For anatomical imaging, a 3D Gradient Echo T2*-weighted sequence covering the entire brain and surrounding tissues was acquired. Slices were acquired using the following parameters: image/matrix size 300 x 210 x 180, field of view = 20 x 14 x 12 mm (for an isotropic resolution of 0.067 mm), repetition time = 35 ms, echo time 6.8 ms, number of signal averages 8. For high resolution T2-weighted RARE scans, the same field of view and matrix size as for T2* and an effective echo time of 43.29 ms, repetition time of 850 ms, RARE factor of 16, and signal averaging of 10. For 3D diffusion tensor imaging (DTI) MRIs, 8 T2-weighted (A0) images and sets of diffusion-weighted (b = 1800 s/mm2) echo planar imaging (EPI) volumes were acquired with diffusion gradients applied in 60 non-collinear directions, producing a total of 68 volumes. The acquisition matrix was 180 × 140 × 144, acquired in 4 segments. The repetition time and echo time for each EPI volume were 400 and 20.6 ms, respectively. The field of view was 18 x 14 x 14.4 mm (field of view saturation slabs were used to null signal derived from outside of the sample field).

In vivo MRI scanning

Mice were initially anaesthetised with 3% isoflurane and secured in an MRI compatible cradle (Rapid Biomedical GmbH, Rimpar, Germany). Anaesthesia was maintained during scanning using 1.5%–2% isoflurane in oxygen/air (50/50, 1 L/min). The respiration rate and rectal temperature were monitored throughout, with body temperature maintained at 37°C (SA Instruments Inc., Stony Brook, NY, USA). Arterial spin labelling (ASL) MRIs were performed using the same MRI scanner as described above for ex vivo scans. Scout images were taken to confirm correct positioning and the magnetic field was optimised using an automated 3D field mapping routine. A 2-dimensional 33-slice T2-weighted (RARE) anatomical scan was performed to identify the scanning depth required for the calcified thalamic regions (0.5 mm slice thickness, image size/data matrix = 260 x 260 pixels, field of view = 18 x 18 mm, repetition time = 3600 ms, echo time = 44 ms, signal averages = 3). For ASL, a flow-sensitive alternating inversion recovery (FAIR) spin-echo EPI sequence was used. A single 1 mm thick slice at the region of interest was selected based on the T2 structural scans (image size = 96 x 96, field of view = 18 x 18 mm, echo time = 10.92 ms). Finally, we acquired a susceptibility-weighted gradient echo scan (SWI, flow compensated FLASH sequence; slices = 33, image size = 180 x 180 pixels, field of view = 18 x 18 mm, echo time = 8 ms, repetition time = 662 ms, averages = 4, flip angle = 30°).

Immunolabeling

For paraffin-embedded sections, mice were perfused with PBS and then perfusion fixed with 4% PFA. Brains and/or peripheral organs were extracted and then immersion fixed in 4% PFA overnight at 4°C. Samples were paraffin embedded before being cut into 5 μm sections. For immunostaining, samples were first dewaxed in xylene and then rehydrated, using standard procedures. Different antigen retrieval methods (using citrate-based [H-3300-250] or tris-based [H-3301-250] antigen unmasking solution) were performed depending on antibody requirements, using a water bath (80-97.5°C for 30 min) to heat sections. Samples were blocked using 10% normal serum (derived from the species of the secondary antibodies) with 0.1% triton x-100 for 1 h. Primary antibodies were applied overnight in 5% normal serum in PBS at 4°C. Primary antibodies included anti-GFAP (2.2B10; 1:500), anti-SERPINA3N (AF4709; 1:100), anti-NeuN (ab177487; 1:400), anti-osteopontin (SPP1, AF808, 1:200), anti-IBA1 (019-19741; 1:2,000), anti-IBA1 (ab178846; 1:500), anti-OLIG2 (AB9610; 1:500), anti-SOX10 (ab155279; 1:1,000), anti-CD206 (AF2535; 1:200) and anti-fibrinogen (A008002-2; 1:500). Samples were repeatedly washed in PBS and then fluorescently conjugated secondary antibodies were applied for 1-2 hr at room temperature (RT) in the dark (1:500, Life Technologies–Molecular Probes). Samples were repeatedly washed in PBS and then counterstained with 1 μm DAPI for 3 min at RT. Sections were repeatedly washed in PBS, then allowed to dry before being mounted with anti-fade mounting medium. Finally, slides were coverslipped and left to cure and protected from light prior to imaging.

For free-floating sections, *Csf1r*$^{\Delta FIRE/\Delta FIRE}$ mice and littermate controls were injected intraperitoneally with 100 μl of pentobarbital and then transcardially perfused with cold PBS with EDTA (1:1000), followed by perfusion fixation with 10% formalin. Brains were then dissected and post-fixed in 10% formalin for 24 hours. Brains were washed with PBS 3 times and cryopreserved in a 20% sucrose solution for 48 hours. After this, brains were frozen using isopentane and stored at -80°C until sectioning. Mouse brains were sectioned coronally using a cryostat. Each brain slice was 40 μm thick and stored at -20°C in an antifreeze solution (250 mM sucrose, 0.1 M PBS solution [Na-PBS, pH 7.4], 7 mM $MgCl_2$, and made to 1 L with glycerol). For immunostaining, brain slices were transferred into well plates and washed 3 times with PBS. Slices were left for 2 hours in blocking solution (10% donkey serum diluted in 2% PBS-Triton). Blocking solution was then removed, and slices were incubated at 4°C overnight in primary antibodies diluted in blocking solution. Primary antibodies included anti-CD13 (AF2335, 1:100), anti-CD31 (553370, 1:500), anti-osteopontin (AF808, 1:200), anti-β-dystroglycan (sc-33702, 1:1000), and anti-ERG (ab92513; 1:1000). After overnight incubation, the primary antibodies were discarded, and the slices washed 3 times with 2% PBS-Triton-X. Brain slices were then incubated for 2 hours, protected from light, in fluorophore-conjugated secondary antibodies (Alexa Fluor 488 [A-21208, 1:1000], 568 [A-11057, 1:1000], and 647 [A-31571, 1:1000]) diluted in blocking solution. Slices were then washed once with 2% PBS-Triton. Nuclei were stained for 5 minutes with Hoechst (1:1000). Slices were washed 3 times with PBS and mounted onto slides using prolong Glass mounting media, stored at 4°C and protected from light until imaged.

For co-staining with bisphosphonates (and for the data shown in Figures S14C and S14D), brains were sectioned with a vibratome (Leica VT1000S) into 60 μm thick slices and stored in 24 well plates in 0.01% NaN_3 in PBS until further processing. Brain slices were blocked overnight in 1% BSA, 0.1% Triton™ X-100 in PBS at 4°C. Slices were then incubated for 3 days at 4°C in primary antibodies in 0.5% BSA, 0.05% Triton™ X-100 in PBS. Brain slices were washed 4-5 times with 0.5% BSA, 0.05% Triton™ X-100 in PBS at RT. Slices were incubated overnight at 4°C with secondary antibodies diluted in 0.5% BSA, 0.05% Triton™ X-100 in PBS. Brain slices were then incubated with AF647-RIS (Biovinc, stock concentration 0.02 nmol/μl in 0.9% NaCl) or 5-FAM-Zol (Biovinc, stock

concentration 0.02 nmol/μl in 0.9% NaCl) prepared at 1:200 dilution in 0.5% BSA, 0.05% Triton™ X-100 in 1X PBS for 2 hours at RT. Brain slices were washed 4-5 times with 0.5% BSA, 0.05% Triton™ X-100 in PBS at RT. Slices were then mounted in ProLong® Gold Antifade (Invitrogen).

Histological staining

Mice were deeply anaesthetized and transcardially perfused with ice-cold PBS followed by perfusion fixation with ice-cold 4% paraformaldehyde (PFA) in PBS. Tissue was post-fixed in 4% PFA and then processed for paraffin embedding. Brains were sectioned into 5 μm thick slices using a Leica microtome. For H&E staining, sections were deparaffinized and rehydrated using alcohol, followed by staining with haematoxylin for nuclei and subsequent counterstaining with eosin for cytoplasmic structures (using standard histological procedures). For Alizarin red staining, samples were incubated in an Alizarin Red S solution for 5 minutes after being dewaxed and rehydrated. Samples were then rinsed, counterstained with 0.05% Fast Green in 0.2% acetic acid for 1 min, and then rinsed again before mounting. For von Kossa staining, samples were incubated in 2% silver nitrate solution and exposed to strong light (after being dewaxed and rehydrated). Samples were then washed in distilled water before being placed in a 5% sodium thiosulphate solution. Samples were washed again and then counterstained with "red" or "green" solution. Samples were washed in distilled water a final time, then dehydrated, cleared in xylene, and mounted. Perl's Prussian Blue Reaction (PBR) staining was performed using a kit from TCS Biosciences (HS652), as per the manufacturer's instructions. For Congo Red staining, slides were stained in Congo Red solution for 5 min, washed in potassium hydroxide for 1-3 min, washed in tap water for 1 min, counterstained with Mayer's haemalum for 1 min, washed in running water for 10 s, blued in Scott's tap water substitute for 30 s, and washed once more under running water for 10 s. Slides were then dehydrated, cleared in xylene, and mounted. Mounting was performed using a DPX mountant (CellPath; SEA-1304-00A).

Microglial transplantations

We previously validated a commercial source of C57BL/6 primary mouse microglia (ScienCell, Catalog #M1900-57) that express high levels of the homeostatic microglia markers P2RY12 and TMEM119 and can be readily transplanted into the brains of haplotype-matched *Csf1r*$^{\Delta FIRE/\Delta FIRE}$ recipient mice.[55] Donor microglia were thawed into commercially available microglial media (ScienCell, Catalog #1901), allowed to recover for 1 h in a 37°C cell culture incubator, and then resuspended in sterile 1× PBS at a concentration of 6,250 cells/μl and placed on ice immediately prior to transplantation.

Microglial transplantations of neonatal mouse pups were performed as previously described.[75] Briefly, P1 *Csf1r*$^{\Delta FIRE/\Delta FIRE}$ pups were placed in a clean cage over a heating pad with a nestlet from the home cage. Pups were then placed on ice for 2–3 min to induce hypothermic anaesthesia. Free-hand transplantation was performed using a 30-gauge needle (7803-07; Hamilton) affixed to a 10 μl Hamilton syringe (7653-01; Hamilton), mice received 1 μl of primary mouse microglia suspended in sterile 1× PBS at 6,250 cells/μl at each injection site (eight sites) totalling 50,000 cells/pup. Bilateral injections were performed at 2/5th of the distance from the lambda suture to each eye, injecting into the lateral ventricles at 3 mm and into the overlying superior cortex at 1 mm, and into the posterior cortex in line with the forebrain injection sites, and perpendicular to lambda at a 45° angle. Transplanted pups were then returned to their home cages and weaned at P21.

At 9-months-of-age, PBS- and microglia-injected *Csf1r*$^{\Delta FIRE/\Delta FIRE}$ mice were perfused with ice-cold 1xPBS and isolated brains were drop fixed in 4% (wt/vol) PFA for 48 h then cryoprotected in a 30% (wt/vol) sucrose at 4°C. Brains were sectioned coronally into 30-μm-thick slices on a freezing microtome (Leica, SM 2010R) cooled to -70°C and stored in a solution of 0.05% NaN_3 (S2002; Sigma-Aldrich) in 1× PBS (P44017-100TAB; Sigma-Aldrich) as free-floating slices. Alizarin Red S (TMS-008, Millipore-Sigma) staining was performed following manufacturer's protocol and imaged using Keyence BZ-X810 Widefield Microscope/Maestro Edge. ImageJ software was used to analyse stained tissue. Antibodies used for immunofluorescence staining on these sections were goat anti-IBA1 (1:300; ab5076; Abcam), mouse anti-SMI312 (1:1000; 837904; biolegend), rabbit anti-NeuN (1:1000; abn78; Abcam), chicken anti-GFAP (1:2000; ab4674; Abcam), goat anti-Olig2 (1:500; AF2418; R&D biosystems), goat anti-SerpinA3N (1:150; AF4709; R&D biosystems), and Ris-647 (1:1000; BV500101; Biovinc). Microglia engraftment and risedronate-positive calcifications were captured using an Olympus FX3000 confocal microscope, and hemibrain stitch assembled using Fluoview FV31S-DT software.

Hematology

To examine the cellular composition of blood from aged *Csf1r*$^{WT/WT}$ and *Csf1r*$^{\Delta FIRE/\Delta FIRE}$ mice, blood was collected in EDTA-coated "microvettes" (Sarstedt, cat# 20.1341.100) and immediately inverted multiple times to prevent clotting. Routine hematology was carried out using an automated analyzer (ADVIA 2120i, Simens). Blood smears were prepared manually, stained with modified Wright-Giemsa, and reviewed by light microscopy by a veterinary clinical pathologist (Easter Bush Pathology, Edinburgh University).

QUANTIFICATION AND STATISTICAL ANALYSIS

Single-cell RNA sequencing analysis

Alignment to the reference genome, feature counting, and cell calling were performed following the 10x Genomics CellRanger pipeline (v5.0.0), using the default mm10 genome supplied by 10x Genomics (https://cf.10xgenomics.com/supp/cell-exp/refdata-gex-mm10-2020-A.tar.gz). From the output, the filtered matrices were used for downstream analyses. Pre-processing was performed

on the University of Edinburgh's compute cluster Eddie. The analysis was performed with R v.4.1.1.(v.4.2.1 for thalamus). Full details to replicate the analysis pipelines described below, including the code and package versions used, can be found in code scripts available on the GitHub repositories linked in the code availability section.

In brief, all the datasets were processed as follows. Cells were first filtered using dataset-specific parameters based on genes and unique molecular identifiers (UMIs) per cell, the ratio between these two parameters and the percentage of mitochondrial gene reads per cell. Thresholds were computed with the isOutlier function from scater,[65] and modified if necessary, to keep them relaxed at this first stage (for details, see Table S1). The gene quality control was also permissive, keeping all genes that were detected in at least two cells. Using scran,[66] the data were normalized by deconvolution, and the top 15% highly variable genes were selected. Following principal component analysis (PCA), between 20 and 30 principal components (PCs) were kept for downstream analysis (cut-off selected by examination of an Elbowplot). Two nonlinear dimensional dimension representation were computed, the t-distributed stochastic neighbour embedding (t-SNE)[76] and the uniform manifold approximation and projection (UMAP).[77] A graph-based clustering approach was used to cluster the cells using the clusterCells function from scran and/or the FindClusters function from Seurat.[67] The cell type identity of each cluster was identified using a combination of canonical marker genes, top expressed genes, and differentially expressed genes between clusters computed with findMarkers from scran. As in Ximerakis et al.[78] we performed a cluster QC, to exclude clusters formed by doublets or low quality cells. We excluded clusters where most cells had low UMI counts or high mitochondrial RNA; protecting clusters that were mostly formed by *Csf1r*$^{\Delta FIRE/\Delta FIRE}$ brain cells, as the difference could be due to their condition; dataset specific thresholds were chosen for these parameters, and they can be found in the GitHub code. The potential doublets were computed with findDoubletClusters from scDblFinder, and the top hits were manually evaluated and selectively excluded. Following this preliminary analysis, a second round of analysis was performed. Cell and gene quality control were further adjusted, this time using not only dataset specific thresholds, but also cell type specific thresholds (for details, see Table S1). The normalisation, feature selection, and dimensional reduction were repeated with the clean datasets following the same procedure described above. Choosing the clustering resolution and performing the cluster annotation were done hand-to-hand, using clustree[69] as a reference to understand the differences between cluster resolutions, and ensuring there was no over-clustering or under-clustering of the different cell types, merging clusters if necessary.

In order to study the differences between *Csf1r*$^{WT/WT}$ and *Csf1r*$^{\Delta FIRE/\Delta FIRE}$ mice, a differential abundance analysis was performed with Milo[21] and differentially expressed genes (DEGs) per cell type and per cluster were computed by pseudo-bulk with edgeR,[79,80] adding the batch as a covariate. As background microglia genes were appearing as differentially expressed between the two conditions we decided to perform an ambient RNA removal from the DEGs lists, using DropletUtils.[70] The first ambient profile was computed with ambientProfileEmpty, and it was then further refined using known microglia genes that should not be expressed in other cell types, using ambientContribNegative in all non-immune cell types. The minimum ambient contribution was calculated by taking the minimum from the two ambient contribution estimates, which was then used for filtering any gene with an estimated contamination proportion greater than 0.25. To investigate the pseudotime trajectories of the oligodendroglia we used Slingshot (v 2.0.0). To focus the analysis, we subsetted for the clusters labelled as mOligo1-4, iOligo, pOPC and OPC. Within this subset, we repeated feature selection and batch correction. For input into Slingshot, we utilised 25 dimensions from the corrected PCA resulting from the fastMNN batch correction method. It is important to note we selected this embedding as the UMAP yield spatially separated clusters, which were not suitable for computing a continuous trajectory. Finally, an interactive application was produced with ShinyCell[72] (link provided in the "data and code availability" section).

The following modifications were performed on the juvenile and thalamus datasets: In the juvenile dataset, one of the batches was of lower quality; therefore, it was disregarded when deciding the QC thresholds by using the "subset" argument in the isOutlier function. In addition, there was a batch effect in this dataset, revealed in the first dimensional reduction and by the gene expression variance explained, computed with scater. Batch correction was performed using mutual nearest neighbours with fastMNN from batchelor.[73] The thalamus fastq reads were aligned to the reference genome with CellRanger v.7.0.0 that also includes intron reads. A sex effect was observed in this dataset and two integration methods were tested to correct for the effect, fastMNN and harmony.[74] Finally, harmony was kept as it yielded a better integration. Due to an unbalanced number of female and male mice between *Csf1r*$^{WT/WT}$ and *Csf1r*$^{\Delta FIRE/\Delta FIRE}$ thalamic samples, differences between these two groups are reduced in the dataset corrected for sex. This affects the dimensional reduction representations and the clustering, which are therefore underestimating the differences between *Csf1r*$^{WT/WT}$ and *Csf1r*$^{\Delta FIRE/\Delta FIRE}$. The DEGs are not affected by this correction, as they were computed back into the raw values, adding the sex as an additional covariate.

The integration between the three ages was performed with fastMNN. The corrected PCs were used to recompute the dimensional reduction and to perform a re-clustering, with the quickClusters function form scran. The cluster annotation was performed using the previously described annotations obtained when analysing the datasets separately. The interaction between the changes in genotype and the changes with aging was assessed for the major cell types with edgeR, by adding an interaction factor to the linear model design.

MRI analysis

Dicom files were exported to NIfTI using FIJI prior to image processing. Brains were computationally extracted from surrounding tissue using a custom MATLAB script. Briefly, the 3D volumes were binarized with a threshold equal to 6 times the signal of surrounding Fomblin. Signal in the skull bone is low and hence included in the negative mask. A spherical element of 5 pixels radius was used to

Please cite this article in press as: Munro et al., Microglia protect against age-associated brain pathologies, Neuron (2024), https://doi.org/10.1016/j.neuron.2024.05.018

dilate the negative mask, which separated the brain tissue signal from other tissues. All unconnected regions were supressed, then the brain mask was dilated using a spherical element of 6 pixels radius to close holes. Finally, the mask was eroded using a spherical element of 2 pixels radius to remove the subarachnoid space. Images were all visually checked, and parameters refined as needed. We re-used the mouse brain MRI atlas from Dorr et al.,[81] which includes 115 lateralized labels. Skull-stripped scans were exported at the same resolution, then we used custom scripts in ANTs to apply the N4 algorithm and perform scan registration to template. Jacobian matrices were then used to warp the labelled atlas into each scan's space.

Volumetry was computed with custom MATLAB scripts using the warped labels. Region volumes were computed as the sum of the voxels of a certain label multiplied by individual voxel size. DTI metrics were recovered from the values computed by Bruker's Paravision 360 software. Briefly, we extracted fractional anisotropy (FA), axial diffusivity (AD) and radial diffusivity (RD). Mean diffusivity (MD) was defined as the sum of AD and RD. Hypointensities were automatically detected independently per region. Voxels whose signal was below the regional median of 3 median absolute deviations (MAD) were considered as hypointensities. Hypointensities closer than 210 μm to the mask border were excluded as border effects and minor field distortions created false positives.

For the arterial spin labelling (ASL) analysis, cerebral blood flow maps were generated using the Bruker software (Paravision 360) using equation [1] as discussed by Belle et al.[82] Measurements were taken from cerebral blood flow (CBF) maps in ImageJ after manually drawing regions of interest based on the in vivo structural T2 scans. CBF measurements were taken using the original/harsh voxels of the CBF maps. For representative ASL images, CBS maps were subsequently smoothed for illustrative purposes using median filtering in ImageJ.

Microscopy and image analysis

For confocal microscopy, Ziess LSM 710 and Leica SP8 confocal microscopes were used with images taken using x5-x60 objectives. For full brain section scans, a Ziess Axioscan was used with images taken using a 20x objective lens. For the free-floating sections, a Leica SP8 confocal microscope with 5 detectors and an Opera Phoenix High Content Screening System was used to image slides.

For the GFAP quantification in Figure 3B, QuPath (version 0.4.3) was used for image analysis. Areas of interest were manually drawn. Total numbers of $GFAP^{high}$ structures (defined based on the use of a consistent intensity threshold) were quantified per area using the Analyze > Cell detection > Cell detection command. For the Neun quantification, QuPath (version 0.4.3) was used for image analysis. Areas of interest were manually drawn. Total numbers of $DAPI^{+}$ nuclei and numbers of $NeuN^{+}DAPI^{+}$ nuclei were quantified per area using the Analyze > Cell detection > Positive cell detection command. Numbers of $NeuN^{+}DAPI^{+}$ nuclei per area were calculated, as well as the percentage of all nuclei that were neuronal (i.e., % of DAPI+ nuclei that were also $NeuN^{+}$). For the alizarin red quantification (in Figure 5B), ImageJ was used to manually draw the thalamic region (using the polygon selection tool). The Threshold > Default > Over/Under > Apply command was then used to define thresholds, and measurements were taken for both the area and the % of area covered by thresholded pixels.

For the quantifications in Figures 5C and 6D, IMARIS (version 9.9) was used for volume rendering of individual channels for the quantification of the numbers of $SPP1^{+}$ structures that were in contact/not in contact with $GFAP^{high}$ astrocytes (Figure 5C) or the vasculature (as labelled by β-dystroglycan; Figure 6D). For the vascular analyses in Figures 6H–6K, the thalamus was subdivided into 4 regions for each animal (dorsal-left and right and ventral-left and right) and a region of 1000x700 μm was analysed, with 3 replicates (slices) per animal (7 $Csf1r^{WT/WT}$ and 7x $Csf1r^{\Delta FIRE/\Delta FIRE}$ mice for a total of 168 images). The images were all analysed using Vas-O-Matic, a homemade ImageJ-based tool used to perform automated analyses of 2D fluorescence microscopy datasets. Vas-O-Matic, through thresholding and particle filtering, segments the vasculature and correlates pericyte coverage to vessel diameter. Vas-O-Matic was used to quantify pericyte coverage (%), vessel diameter (μm), and vascular density (mm^3) as independent results.

Statistical analyses

Sample sizes and statistical tests used for each experiment are provided in respective figure legends. Significance was defined as P (or adjusted P) < 0.05. Experimenters were blinded where possible. Statistical methods were not used to pre-determine study group sizes. Statistical analyses were performed using GraphPad Prism (version 10), unless otherwise stated in respective methods sections. Data are expressed as biologically independent samples with mean ± S.E.M. unless indicated otherwise. Full two-way ANOVA test statistics tables can be found in Table S4.

ADDITIONAL RESOURCES

Interactive database

For an interactive database to mine single-cell RNA sequencing datasets produced for this manuscript, please use the following link: https://annawilliams.shinyapps.io/shinyApp_jpriller/